Green Chemistry

PAPER

View Article Online
View Journal

Check for updates

Cite this: DOI: 10.1039/d6gc00489j

Valorization of consolidated bioprocessing residues for bioplastics

Nataraja S. Yadavalli, [a,d] Mohammad Aghajohari, [a,d,f] Neal N. Hengge,[b] Daniel C. Josey,[a,d] Jacob Dempsey,[b] Jacob K. Kenny,[b] Bruno C. Klein, [b] Rebecca J. Hanes, [b] Evert K. Holwerda,[c] Yannick J. Bomble,[b] Kush G. Patel, [a] Jason J. Locklin, [a,e] Sergiy Minko [a] and Breeanna R. Urbanowicz *[a,d,e,f]

This study demonstrates an organic solvent-free processing strategy to valorize consolidated bioprocessing (CBP) residues, from switchgrass and poplar biomass, into functional poly(butylene succinate) (PBS)-based biocomposites using high-shear homogenization (HSH). HSH transformed the switchgrass and poplar CBP residues (CBP-R) into fine, uniformly distributed particles and microfibers. The composites of PBS with homogenized switchgrass residues (H-CBP-R-SG) or homogenized poplar residues (H-CBP-R-P) at a 70/30 weight ratio exhibited improved processability and mechanical integrity, with the Young's modulus for the PBS/H-CBP-R-SG and PBS/H-CBP-R-P nearly doubling to 0.66 ± 0.07 GPa and 0.65 ± 0.04 GPa, respectively, compared to neat PBS (0.36 ± 0.02 GPa). Dynamic Mechanical Analysis (DMA) reveals a significant suppression of the tan δ peak magnitude, indicating that HSH-mediated physical activation facilitates stress transfer in composites typical of covalent chemical grafting systems. While the transition to a stiffness-dominated profile reduces ductility, the resulting composites exhibit the dimensional stability and resistance to thermal warping required for high-fidelity FDM 3D printing and injection molding. Beyond material performance, comprehensive techno-economic analysis (TEA) and life cycle assessment (LCA) confirmed that diverting CBP residues into composite products can improve the economic viability of the biorefinery without substantially increasing biorefinery global warming potential (GWP). At a 30 wt% blend ratio, incorporating residuals into PBS yielded a minimum selling price for the composite of $4.07 per kg compared to the conventional bioplastic price of $5.00 per kg. This approach aligns with circular bioeconomy principles by converting waste streams into value-added products. Furthermore, this innovative strategy addresses key challenges in bioplastic development, including cost, compatibility, and performance, while simultaneously advancing waste minimization strategies for sustainable manufacturing systems.

Received 23rd January 2026,
Accepted 20th May 2026

DOI: 10.1039/d6gc00489j

rsc.li/greenchem

Open Access Article. Published on 21 May 2026. Downloaded on 6/11/2026 11:23:03 PM.
This article is licensed under a Creative Commons Attribution 3.0 Unported Licence.

Green foundation

1. This work advances green chemistry by establishing an organic solvent-free, scalable *waste-to-wealth* framework converting underutilized consolidated bioprocessing (CBP) residues into structural bio-composites. Prioritizing high-shear homogenization over traditional chemical functionalization demonstrates that mechanical energy acts as a minimalist, cleaner alternative to covalent modification strategies.
2. We engineered lignin-rich fillers *via* HSH, imparting robust interfacial stress transfer and chain immobilization without auxiliary solvents. Ashby mechanical mapping confirms that this physical pathway elevates low-value residues into the general engineering component regime, offering sustainable, cost-competitive replacements for commodity fossil-based polymers like polypropylene.
3. To overcome industrial energy bottlenecks, future studies could replace thermal spray drying with energy-efficient mechanical dewatering like industrial pressure filtration. Transitioning to fully bio-derived polymer matrices and analyzing long-term biodegradation and chemical recycling kinetics would maximize a closed-loop material circularity.

[a]*University of Georgia, Athens, GA 30602, USA. E-mail: breeanna@uga.edu*
[b]*National Laboratory of the Rockies, Golden, Colorado, USA*
[c]*Thayer School of Engineering, Dartmouth College, Hanover, USA*
[d]*Complex Carbohydrate Research Center, University of Georgia, Athens, GA 30602, USA*
[e]*New Materials Institute, University of Georgia, Athens, GA 30602, USA*
[f]*The Plant Center, University of Georgia, Athens, GA 30602, USA*

1. Introduction

Renewable biofibers can be combined with thermoplastic polymer matrices to produce biocomposites with enhanced properties tailored for diverse industrial applications.[1–3] Traditionally, non-biodegradable fossil-based plastics such as polyethylene, polypropylene, and polystyrene have been

Open Access Article. Published on 21 May 2026. Downloaded on 6/11/2026 11:23:03 PM. This article is licensed under a Creative Commons Attribution 3.0 Unported Licence.

favored for their durability, thermomechanical properties, and low production costs. However, there is a growing interest in sustainable alternatives due to environmental concerns. Among these, synthetic biodegradable polymers like poly(lactic acid) (PLA), poly(butylene succinate) (PBS), and polybutylene adipate terephthalate (PBAT) have gained prominence for their potential to mitigate the negative impacts of petrochemicals. Despite their promise, these bioplastics face challenges, such as high production costs and distinct mechanical properties compared to conventional plastics. Moreover, many of these materials, including PLA and PBS, only meet target biodegradation kinetics under industrial composting conditions, limiting their environmental benefits.

Composites incorporating lignocellulosic (LC) biomass represent an area of increasing interest. These products integrate renewable, low-cost, biodegradable natural fibers or fillers into carrier polymer matrices to produce partially bioderived materials that are functionally equivalent to incumbent fossil-derived materials.[4,5] Composites reinforced with plant biomass have found applications in the automotive, construction, and packaging industries where sustainability is emphasized.[6,7] Our prior studies have shown that plant biomass-derived hemicelluloses from industrial waste streams can be modified and processed into biocomposites with improved moisture barrier performance.[8] Furthermore, thermoplastics with environmental issues at their end-of-life, including recyclability, can be upgraded into self-disintegrating biocomposites by incorporating spore-bearing bacteria into the polymer matrix.[9] Unfortunately, plant fibers lack plastic behavior, and often suffer from relatively poor compatibility with hydrophobic polymer matrices leading to strong segregation and compromising the overall biocomposite performance.[10] Processing difficulties, such as clogging of extrusion equipment, the need for compatibilizers, and heterogeneous distribution of LC biomass particles in the polymer matrix, are common issues that can compromise both material and mechanical properties.[11–14] Plasticizers and compatibilizers such as maleic anhydride grafted polypropylene or polyethylene,[15] glycerol,[16] furfural,[17] citric acid,[18] triethyl citrate,[19] and epoxide soybean oil,[20] have been explored to generate LC biomass composites to improve composite blending, extrusion, and expand potential downstream applications. Further, various fiber surface modification techniques like alkali treatment, silane coupling, and enzymatic modification have been employed to enhance compatibility and mechanical properties.[21–23] However, these strategies often prove cost-ineffective and difficult to scale for industrial bioplastic production.

Industrial utilization of biomass often generates substantial waste streams. These side streams are often underutilized by-products that represent untapped resources for the production of biocomposites.[24–26] Consolidated bioprocessing (CBP), which integrates biomass saccharification and fermentation into a single step, is a biological process used to efficiently convert lignocellulosic feedstocks to biofuels or chemicals. Despite its efficiency, CBP often generates residual biomass waste streams containing enzymatically deconstructed biomass with altered structural and chemical properties.[27,28] Processing lignocellulose by CBP physically alters the residual material, demonstrated by an 8-fold reduction in viscosity of the solids slurry during the first 10% of carbohydrate solubilization and a 2000-fold reduction overall.[29] These residuals also tend to be finer, which may facilitate better processibility, dispersion, and integration into the polymer matrix. Thus, by making structural components more accessible through CBP, these residuals provide a distinct advantage over traditional feedstocks in the manufacturing of composites. Furthermore, the selective removal of carbohydrates leaves a lignin-rich residue, which lowers the hydrophilicity of the biomass, mitigating moisture-related processing and mechanical performance issues in thermoplastic composites. Thus, utilization of CBP residuals aligns well with circular bioeconomy principles by maximizing the value derived from biorefineries and reducing waste streams.[30]

Among biodegradable bioplastics, PBS offers a unique combination of properties that make it particularly suitable for composite production, including compatibility with natural fibers, low melting temperature, and processing flexibility.[31] PBS can be synthesized from both petroleum- and bio-based monomers, including bio-derived succinic acid and 1,4-butanediol, offering pathways towards green polymer production.[32,33] Various synthesis methods, copolymerizations, and blending approaches have been explored to tailor PBS's thermal, mechanical, and biodegradability properties, further expanding its applicability in packaging, agriculture, biomedical devices, and other fields.[34–37] Research has demonstrated that PBS-based biocomposites, reinforced with natural fibers, exhibit improved tensile strength, modulus, and thermal properties compared to neat PBS.[38–43] Additionally, there has been significant interest in the biodegradation behavior of PBS/plant biomass composites, revealing that inclusion of natural fibers often accelerates biodegradability by promoting microbial activity and hydrolytic degradation.[30,44,45]

Processing techniques, including melt extrusion and injection molding, have been effectively employed to fabricate PBS-based composites with plant biomass fillers.[5,46,47] In the realm of additive manufacturing, the incorporation of LC biomass fibers into PBS to produce thermoplastic filaments for 3D printing enhances the mechanical performance and sustainability of printed parts.[48] For instance, incorporation of cocoa bean shell residues into the PBS matrix has been shown to improve the disintegration rate under composting conditions for both molded and printed composites. PBS alone exhibits a disintegration of 1.8% and 4.7% for the injected and printed samples, respectively. While the addition of 20 wt% natural fibers results in a 48% and 53.4% disintegration rate for composites prepared *via* injection molding and printing, respectively.[49] However, several challenges still remain, including non-uniform filler dispersion, caramelization and agglomeration of biomass particles, and poor interfacial adhesion, necessitating careful control of processing

 This journal is © The Royal Society of Chemistry 2026

Open Access Article. Published on 21 May 2026. Downloaded on 6/11/2026 11:23:03 PM.
This article is licensed under a Creative Commons Attribution 3.0 Unported Licence.

conditions.[47,50] Similarly, injection molding of PBS and plant biomass composites allows for the fabrication of structurally robust components with improved stability and tailored biodegradation rates, necessary for sustainable manufacturing practices.[5,46,51]

In this study, we developed PBS-based thermoplastic composites using CBP residuals as LC-derived reinforcing agents. To enhance the dispersion and interfacial bonding of composites, we developed a mechanical processing strategy involving milling and high shear homogenization (HSH) to generate uniformly distributed biomass particles and microfibers (Fig. 1). By utilizing HSH in lieu of traditional chemical functionalization, we establish a design principle that prioritizes mechanical interlocking and physical surface activation over energy-intensive chemical modifications. Two key green chemistry advantages of our approach are the elimination of auxiliary organic solvents and the incorporation of renewable plant-derived feedstocks from available bioprocessing waste streams.[52] Our mechanical processing workflow allowed us to achieve significant interfacial integration and polymer chain immobilization through physical rather than synthetic means. We demonstrated that this approach can generate highly uniform composites with enhanced processability that, based on their thermomechanical properties, have potential applications in injection molding and 3D printing. Furthermore, we conducted techno-economic analysis (TEA) and life cycle assessment (LCA) to assess the impact on ethanol selling price and global warming potential (GWP) of producing composite materials from CBP residuals and found that as co-products, they benefit the CBP biorefinery by increasing revenues and decreasing the flow of solid material to the boiler without substantially increasing GWP. Furthermore, we found that composite production costs were dominated by capital equipment costs due to the high cost of processing equipment, such as homogenizers and spray driers; however, increasing the solids content during processing substantially decreases equipment capacity requirements and, consequently, costs. Ultimately, the incorporation of CBP residuals has the potential to decrease the price of producing composites, and while we focused our studies on PBS as the primary matrix, this processing strategy is broadly applicable to other industrial plastics and composite formulations.

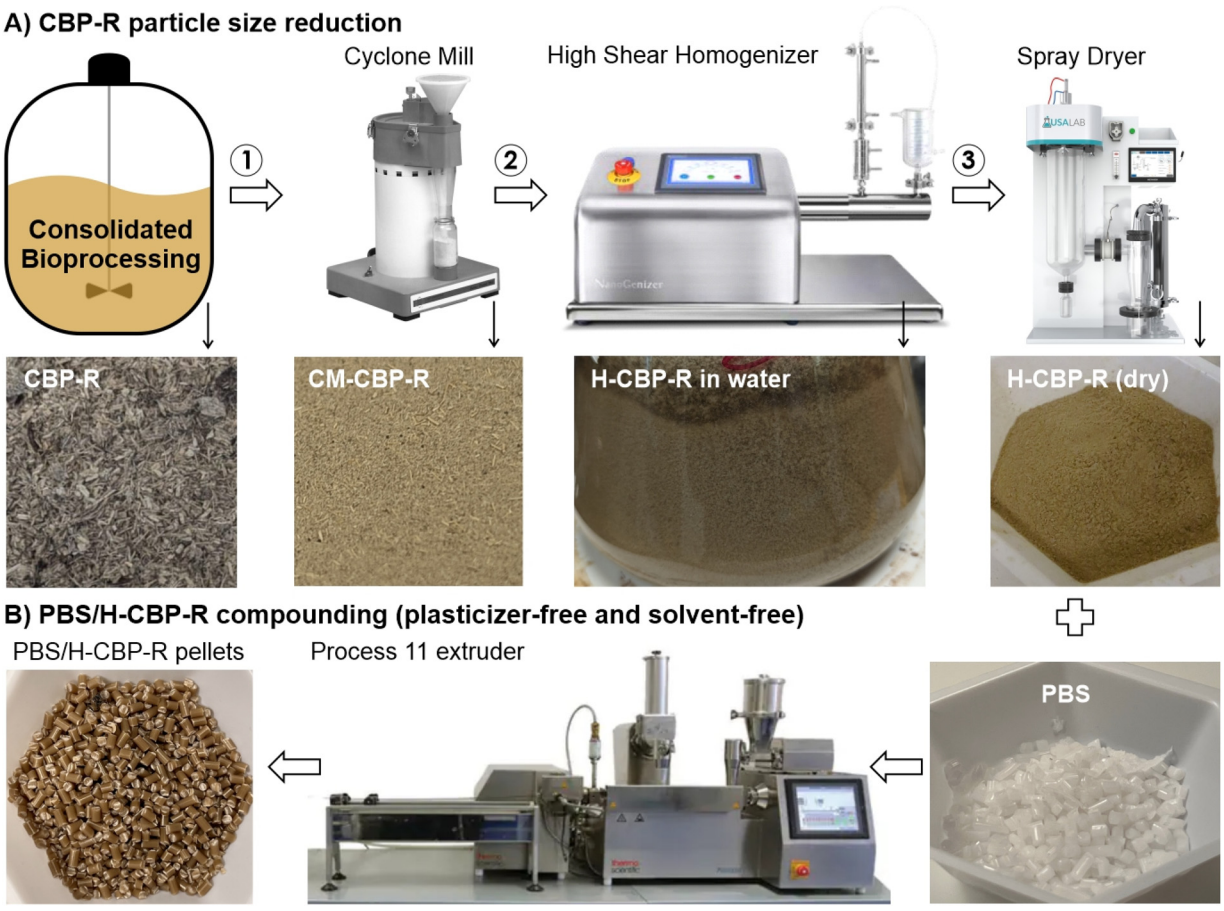

Fig. 1 Schematic representation of the valorization process for Consolidated Bioprocessing residuals (CBP-R) into bio-composite pellets. (A) Mechanical size reduction of CBP-R is carried out using a cyclone mill (CM) followed by high-shear homogenization (HSH) then spray dried. (B) Dry homogenized CBP residuals (H-CBP-R) are compounded with poly(butylene succinate) (PBS) pellets in a melt twin-screw extruder to yield bio-composite pellets.

Open Access Article. Published on 21 May 2026. Downloaded on 6/11/2026 11:23:03 PM. This article is licensed under a Creative Commons Attribution 3.0 Unported Licence.

2. Experimental section

2.1. Preparation of CBP residues (CBP-R)

Clostridium thermocellum was utilized to carry out CBP on unpretreated lignocellulosic biomass at the National Laboratory of the Rockies (NLR) using BioEnergy Science Center (BESC) switchgrass and Center for BioEnergy Innovation (CBI) poplar as feedstocks.[53] Switchgrass and poplar fermentations[54] were carried out at 60 g L^{-1} and 30 g L^{-1} solids loadings, respectively, at 10 L scale in pH controlled bioreactors in the presence of *C. thermocellum* to obtain primary fermented CBP residuals. Briefly, switchgrass and poplar were milled to −20/+80 mesh (0.841 mm–0.177 mm), loaded into 10 L vessels, and then the volume brought up to 4 L with deionized water. Bioreactors were sealed and sterilized in an autoclave at 121 °C for 60 min. Medium for Thermophilic Clostridia (MTC) was prepared according to Holwerda, *et al.*[55,56] at 2× concentration and 5 L was added to each reactor, leaving 1 L of volume for inoculum. *C. thermocellum*, from an Avicel-grown seed culture, was inoculated into bioreactors (BioFlo 310, New Brunswick) containing biomass and MTC at pH 7.0 and fermented for 120 hours. Cultures were maintained at pH 7.0 using 5 M KOH and H_2SO_4, at 55 °C, undergoing agitation using Rushton impellers (250 rpm), with N_2 sparging through the headspace. CBP residuals were recovered by centrifugation of the post-fermentation material at 8000 rpm for 20 min. The supernatant was decanted from the solid residuals, and the solids were then washed 3 times with deionized water. The washed solid residuals were dried at 50 °C for 5 days in a convection oven. Pre- and post-fermented biomass samples were analyzed for chemical composition using methods outlined in the NLR Laboratory Analytical Procedure "Summative Mass Closure".[57] Raw BESC standard switchgrass contained 29.9% glucan, 18.7% xylan, and 15.3% lignin and CBP-R switchgrass residuals were composed of 28.5% glucan, 18.8% xylan, and 25.2% lignin. Raw CBI standard poplar contained 46.7% glucan, 15.8% xylan, and 23.79% lignin, and the CBP-R poplar residuals comprised 41.1% glucan, 14.7% xylan, and 22.8% lignin. Total solids solubilization was calculated by subtracting the dried fermentation residual mass from the initial solids mass loaded into the bioreactor and dividing by the initial solids mass. Solubilization occurring non-biologically was calculated by autoclaving each raw substrate at the same solids loading as the fermented biomass, and then subjecting it to 5 days at 55 °C with no inoculation of *C. thermocellum*. For BESC switchgrass, total solids solubilization was 46.6% and for CBI poplar, total solids solubilization was 7.8%. CBP-processed biomass solids are denoted by "-R" for residuals (CBP-R).

2.2. Biomass processing

A cyclone sample mill (CM) from UDY corporation (USA) was used for initial size reduction of CBP-R to reduce oversized particles and impurities to below ≤200 μm size. To further decrease particle size and achieve a nanoscale fiber morphology, CM processed CBP-R material was processed in DI H_2O using a Nanogenizer-II high shear homogenizer from Genizer LLC (USA) with H30Z (channel diameter 200 μm) and F20Y (channel diameter 75 μm) diamond interaction chambers connected in series (Fig. 1). A slurry of 2% solids of CBP-R in water was subjected to multiple passes until resistance flow subsided at or above 15 000–20 000 psi with a 60% flow rate. Homogenized material was finally dried either by lyophilization or using an In-SD mini spray dryer model (USALAB) with the air-in temperature of 90 °C, feed flow of 10 mL min^{-1}, and a 5 s needle frequency. HSH-processed samples are denoted by "H-" (*i.e.*, H-CBP-R).

2.3. Composite preparation

Injection molding grade BioPBS™ (FZ71, Mitsubishi Chemicals America) was used as the polymer matrix for composite fabrication. According to the datasheet of the manufacturer, the polymer has a melt flow index (MFR) of 22 g per 10 min measured at 190 °C and 2.16 kg (ISO 1133), a density of 1.26 g cm^{-3} (ISO 1183), and a melting point (T_m) of 115 °C. PBS/H-CBP-R composites were fabricated using a solvent-free melt-mixing process. Briefly, dry biomass (30% w/w) was first mixed with PBS in a high-speed grinder using dry ice, followed by drying in a vacuum oven for 48 h at 60 °C. The obtained particle mix was then compounded using a Process 11 Twin-screw Extruder (Thermo Fisher Scientific, USA). Processing conditions were set to minimize caramelization and promote homogeneous dispersion and continuous phase distribution between H-CBP-R and PBS. No plasticizers were incorporated into the composite formulation.

2.4. Pelleting, injection molding, filament extrusion and 3D printing

PBS-based composites were pelletized and flushed through a Process 11 Twin-screw Extruder (Thermo Fisher Scientific, USA), with barrel zones maintained at 125 °C, followed by processing with the HAAKE Minilab II conical twin screw extruder (Thermo Fisher Scientific, USA). The extrudate was then collected in a heated barrel for subsequent injection molding using a HAAKE Minilab II ram injection molder (Thermo Fisher Scientific, USA). The mold temperature was set to 45 °C, with an injection pressure of 350 bar for neat PBS and 700 bar for the composite blends. Specimens were produced for both tensile and Izod impact testing. The compounded melt mixture was pelletized and subsequently processed into 1.75 mm diameter filaments for 3D printing applications using a customized DIY Filastruder/Filawinder filament extrusion system and Mk3s 3D printer equipped with an E3D Obsidian 0.6 mm nozzle (Prusa Research, Austria).

2.5. Scanning electron microscopy

Scanning electron microscopy (SEM) was employed to determine the LC particle size to monitor processing and image the surface morphology of the composites. Imaging was performed using a JEOL JSM-6010LV scanning electron microscope (JEOL USA Inc, USA) housed at the University of Georgia's Complex Carbohydrate Research Center. This instru-

 This journal is © The Royal Society of Chemistry 2026

Open Access Article. Published on 21 May 2026. Downloaded on 6/11/2026 11:23:03 PM. This article is licensed under a Creative Commons Attribution 3.0 Unported Licence.

ment is equipped with a low-vacuum mode, which mitigates charging effects commonly encountered with non-conductive samples such as CBP-R and PBS/H-CBP-R composites, eliminating the need for conductive metal film sputter coating, and thereby preserving the native surface topography of the specimens.

2.6. Thermal properties characterization

Thermogravimetric analysis (TGA) was conducted using a TA Instruments Discovery Series TGA to evaluate the thermal degradation behavior of PBS/H-CBP-R biocomposites. Briefly, samples (7–12 mg) were placed in platinum pans and heated from room temperature to 800 °C, at a constant heating rate of 10 °C min^{-1}, following ASTM standard E2550.

Differential scanning calorimetry (DSC) was performed using a TA Instruments DSC 250 system to analyze the thermal transitions of the biocomposites according to ASTM standard D3418, with all heating and cooling ramps set at 10 °C min^{-1}. Briefly, samples (4–7 mg) were enclosed in aluminum T-zero pans, and subjected to the following temperature cycling protocol: first equilibrium at −80 °C, followed by heating to 200 °C, cooling back to −80 °C to remove thermal history, reheating to 200 °C, and finally cooling to −80 °C.

2.7. Melt flow rate (MFR)

MFR, also known as Melt Flow Index (MFI), was determined using an MP12000 Melt Flow Indexer (Tinius Olsen, USA), adhering to ASTM D1238. Briefly, up to 3 grams of PBS/H-CBP-R composite pellets were heated at 190 °C in the furnace to achieve a molten state. A 2.16 kg weight was then applied to extrude the molten polymer through a die. The extrusion rate was measured and reported in grams per 10 minutes (g per 10 min).

2.8. Mechanical characterization

Tensile testing of composites was performed using an Autograph ASG-X universal testing machine (Shimadzu, Japan) equipped with a 1 kN load cell. Samples were prepared according to ASTM D638, and a controlled tensile (pulling) force was applied. Samples (ASTM D638 Type V bar; n = 5, gauge length of 7.62 cm, with a thickness and width of ∼3.2 mm at the narrow section) were tested at a rate of 20 mm min^{-1}.

Izod Impact resistance was analyzed using a Model 104 Impact Tester (Tinius Olsen, USA) on notched samples (n = 3, 3.1 mm × 12.6 mm × 64 mm, notch depth = 10.2 mm) prepared in accordance with ASTM D256, with a pendulum nominal impact energy of 2.82 J. Samples were aged for 5 days prior to analysis to ensure stress relaxation and moisture equilibration.

Dynamic mechanical analysis (DMA) was performed using a TA Instruments DMA Q800 in tensile mode. Prior to testing, all samples were aged under ambient conditions for 7 days to ensure equilibration. Rectangular specimens with approximate dimensions of 100 mm × 35 mm × 1 mm were used. Measurements were conducted over a temperature range from −90 to 70 °C at a constant frequency of 1 Hz. A strain amplitude of 0.1% was applied, with a preload force of 0.0100 N and a force track setting of 125%.

2.9. Process modeling and techno-economic analysis (TEA)

Process modeling and TEA were conducted in accordance with our previously described publications.[58] A steady process model was developed in Aspen Plus® version 14 for both the CBP biorefinery and the composite production facility. The CBP model was developed starting from the 2011 dilute acid NLR process model, in which pretreatment, enzymatic hydrolysis, and ethanol fermentation of sugars were replaced with CBP equipment as in previous reports.[59] Outputs of the process model, namely the mass and energy flowrates, were used to size equipment and calculate the material input requirements and corresponding costs, which constitute the inputs to the TEA. Capital equipment costs were sourced by adapting previously disclosed vendor quotes. TEA was conducted using a project lifetime of 30 years and an internal rate of return of 10%. Results are presented in the cost year 2020 US Dollars.

2.10. Life cycle assessment (LCA)

A cradle-to-gate LCA was performed to quantify life cycle global warming potential (GWP): emissions of CO_2, CH_4, and NO_2, converted to units of CO_2e using 100-year GWP factors,[60] due to production of ethanol, lignin residuals, and electricity from the CBP biorefinery. Nine scenarios with varying amounts of lignin residual production were modeled to examine the impact of residual diversion on biorefinery life cycle metrics (Table 1). A second cradle-to-gate LCA was performed to quantify life cycle GWP for production of the residual-based composite. A variety of polymer matrices sourced from both fossil and biomass feedstocks (Table 2) were modeled as inputs to composite manufacturing to explore the impact of polymer matrix selection on life cycle metrics of the residual-based composite. Complete life cycle inventory (LCI) datasets for the biorefinery and composite production are provided in the SI (Tables S1 and S2). The DATASMART package, which combines Ecoinvent v2 process data with U.S.-based electricity grid information,[61] was used as the background LCI database. LCA calculations were performed using SimaPro software.

Table 1 The CBP biorefinery coproduces ethanol, lignin residuals, and electricity in varying amounts depending on the amount of residual diverted to composite production

Percentage of residuals to composites	Ethanol production (kg h^{-1})	Residual production (bone dry kg per h)	Electricity production (kWh h^{-1})
0%	23 583	0	16 928
9.4%	23 583	2001	13 551
10%	23 583	2152	13 297
20%	23 583	4303	9667
30%	23 583	6454	6067
50%	23 583	10 757	0
70%	23 583	15 060	0
78.2%	23 583	16 825	0
100%	23 583	21 513	0

Open Access Article. Published on 21 May 2026. Downloaded on 6/11/2026 11:23:03 PM. This article is licensed under a Creative Commons Attribution 3.0 Unported Licence.

Table 2 Eight polymer matrices produced from fossil or biomass feedstocks were modeled as inputs to composite production

Polymer matrix type	Feedstock for polymer matrix	Data source
HDPE	Fossil	DATASMART[61]
LDPE (granulate)	Fossil	DATASMART
LDPE (resin)	Fossil	DATASMART
PET (amorphous)	Fossil	DATASMART
PET (bottle grade)	Fossil	DATASMART
PLA	Biomass	DATASMART
PBS	Fossil	Tecchio *et al.* (2016)[62]
PBS	Fossil	Ioannidou (2022)[63]
PBS	Combined Fossil and Biomass (various agricultural residues)	Tecchio *et al.* (2016)[62]
OBS	Biomass (food waste)	Rajendran and Han (2023)[64]

Both LCAs included a previously developed process model of commercial-scale poplar agriculture.[65] This model included all agricultural and logistical operations for a seven-year poplar harvest cycle: site preparation, seedling production, cultivation, harvest, transportation, and size reduction at the biorefinery. Post-harvest operations to prepare the land for a second harvest cycle or for another land use (*e.g.*, stump removal, soil tillage, *etc*.) were not included in the scope, nor was long-term biomass storage at the biorefinery. At the CBP biorefinery and composite manufacturing facility, all material and energy inputs and coproducts are within scope. All biogenic carbon fluxes are excluded from the scope due to the inherent uncertainty in carbon uptake by poplar agriculture.

Both lignin residuals and electricity can be coproduced by the CBP biorefinery under certain residual diversion scenarios (Table 1). Coproduct allocation using the economic value was applied to allocate total biorefinery life cycle emissions among the three coproducts. The prices used for economic allocation are the same as those used in the TEA, with ethanol price varying with the percentage of residuals diverted to composites and the electricity and residual's prices remaining constant. Economic allocation was used because the three coproducts do not share physical characteristics that could be used for allocation (mass, volume, carbon content), except for energy content. However, energy-based allocation was not used because the lignin residual coproduct is used as a material feedstock rather than as an energy carrier.

3. Results and discussion

3.1. Biomass pre-processing and morphological transformation

Recent research on PBS/lignocellulosic composites has been focused on overcoming weak fiber-matrix bonding and poor dispersion, which have been shown to negatively impact mechanical properties. Therefore, we and others have hypothesized that high-energy mixing, will improve particle distribution in the PBS matrix and will be beneficial for the mechanical properties of the composites. Additionally, the decrease in particle size will minimize the local stress at the LC–PBS interface.[10,66] Studies show that smaller particle sizes (*e.g.*, 45 μm) combined with high mixing speeds enhance delignification and biomass conversion.[67] Others have shown that homogenization techniques, such as Ultra-Turrax at 12 000 rpm, have proven effective for producing well-dispersed cellulose nanofiber suspensions for PBS bionanocomposites.[68] This evolution toward integrating surface treatments with high-energy methods reflects a clear trend aimed at minimizing fiber agglomeration and achieving uniform dispersion in the polymer matrix. This study expands on this work by utilizing HSH to activate the fiber surface. By replacing traditional chemical functionalization with HSH, we implemented a solvent-free design strategy that prioritizes mechanical interlocking over chemical modifications. Furthermore, most chemical modification strategies rely on organic solvents, synthetic additives, and toxic reagents, increasing the environmental burden of material production. On the contrary, our approach provides a pathway for enhancing interfacial integration through physical rather than chemical means. Here, we explored the potential of incorporating CBP residuals into PBS using this approach to yield biocomposite pellets (Fig. 1).

Based on the chemical composition numbers from raw and fermented biomass, total carbohydrate conversion was 53.5% for BESC switchgrass and 10.4% for CBI poplar for once-fermented CBP residuals. Analysis of the particle size distribution of switchgrass and poplar CBP-R revealed a coarse particle size distribution ranging from 1 to 5 mm (Fig. 2a and e). Thus, we utilized a Cyclone Mill (CM) for preliminary size reduction, with a mesh size of 250 μm, effectively reducing particle size to below 200 μm (Fig. 2b and f). To achieve nanoscale fiber morphology, we next applied HSH that relies on intense impact, shear, and energy dissipation forces to further process premilled CBP-R.[69] To achieve this, the CBP-R slurry was subjected to multiple passes through HSH diamond interaction chambers under very high pressure. As the suspension is forced through this restricted opening, the rapid pressure reduction, combined with the high velocity, causes cavitation, turbulence, and immense shear stresses, effectively disrupting the cell walls and disaggregating fiber bundles. CBP-R subjected to HSH showed distinct morphological transformation, which varied based on the biomass type (Fig. 2). Specifically, switchgrass CBP-R residues were present as discrete, elongated fibers, indicating that this material underwent effective defibration (Fig. 2c). Analysis of HSH-processed poplar CBP-R by SEM showed that it reconstituted into two-dimensional flat flakes with a length of 10–100 μm (Fig. 2f and SI Fig. S2). This varying morphological response between the two biomass types likely stems from inherent differences in the hierarchical structure of their respective cell walls, including composition, architecture, and mechanical properties. In the case of poplar CBP-R, high amounts of glucan[70,71] likely lead to delamination along cellulose sheets to dominate in mechanical disintegration. On the other hand, xylan-lignin crosslinks by ferulate esters[72] in switchgrass CBP-R likely result in formation of

 This journal is © The Royal Society of Chemistry 2026

Open Access Article. Published on 21 May 2026. Downloaded on 6/11/2026 11:23:03 PM.
This article is licensed under a Creative Commons Attribution 3.0 Unported Licence.

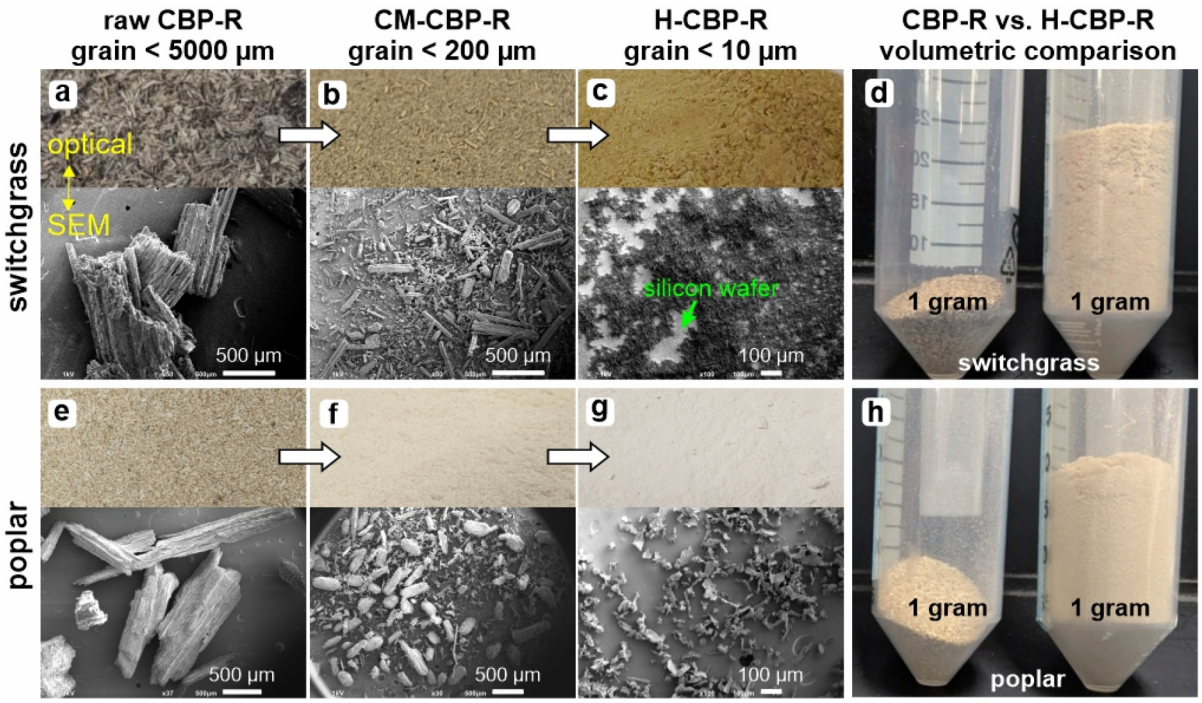

Fig. 2 Comparative analysis of processed CBP residuals from poplar and switch biomass. (a) Raw CBP-R switchgrass and corresponding SEM image. (b) Cyclone milled CBP-R-SG with grain size reduced to below 200 μm. (c) Homogenized and dried CBP-R-SG with fine LC fibers. (d) Comparison of volumetric changes between the switchgrass raw and homogenized CBP-R. (e) Raw CBP-R poplar and corresponding SEM image. (f) Cyclone milled CBP-R-P with grain size reduced to below 200 μm. (g) Homogenized and dried CBP-R-P with reconstituted LC fibers in the form of flat flakes. (h) Comparison of volumetric changes between the switchgrass raw and homogenized CBP-R. Each image has two parts. The top portion of each image is optical image of biomass and the bottom section is the corresponding SEM image.

microfibril bundles that may disintegrate by fibrillar separation after HSH.[69] However, the ability to precisely control and predict such morphological outcomes is complex. Fig. 2d and h shows the volumetric changes that occur after homogenization of CBP-R biomass for switchgrass and poplar, respectively. In Fig. 2d (switchgrass) and Fig. 2h (poplar), the left tube (raw) occupies a compact, smaller volume, while the right tube (homogenized) shows a dramatic increase in volume. This expansion results from homogenization, which reduces the biomass particles into fine, low-density fibers that trap air and resist tight packing.

3.2. Biocomposite formulation and pellet production

Many studies have investigated biocomposites with weight ratios of 90 : 10, 80 : 20, and 70 : 30 of PBS to plant biomass to understand their enhanced properties and applications, and 70 : 30 was previously shown to be optimal.[40,73,74] We utilized a twin-screw melt extruder to produce polymer blends with a 70 : 30 weight ratio, as it facilitates intense mixing and shear, ensuring a homogeneous dispersion of filler within the molten PBS matrix (Fig. 3). Next, we examined the extruded filaments using scanning electron microscopy (SEM) to investigate the impact of the different processing techniques on filler morphology and its integration within the PBS matrix. As expected, the surface of the neat PBS filament (Fig. 3b) is smooth and featureless. In contrast, the surfaces of the CM-processed filaments are highly corrugated and display pronounced topological irregularities, where large, protruding biomass bundles are apparent (Fig. 3e and k). These surface clusters indicate poor wetting and a lack of depth-integration, which can lead to nozzle clogging during 3D printing. Conversely, the HSH-processed filaments exhibit a more refined and uniform surface morphology with no large protrusions (Fig. 3h and n), demonstrating that HSH processing allows the biomass to remain fully encapsulated within the PBS sheath during extrusion. A closer examination of CM-*versus* HSH processed switchgrass residuals reveals the morphological consequences of relying solely on mechanical milling (Fig. 3l and o). Unlike the homogenized samples, the CM particles remain as cohesive fiber bundles with intact cell wall structures with visible micro-gaps and poor wetting (Fig. 3l). Together, these data demonstrate that the HSH process results in microstructural refinements that transform rigid bundles that would otherwise act as stress concentrators into high-aspect-ratio reinforcing agents.

3.3. Thermomechanical analysis and interfacial evaluation

Next, we performed dynamic mechanical analysis (DMA) to quantitatively compare the impact of HSH and CM on mechanical stability, interfacial adhesion, and polymer miscibility. Injection-molded composite films were cut into 10–15 mm specimens for analysis (Fig. 4a). The magnitude of

Open Access Article. Published on 21 May 2026. Downloaded on 6/11/2026 11:23:03 PM.
This article is licensed under a Creative Commons Attribution 3.0 Unported Licence.

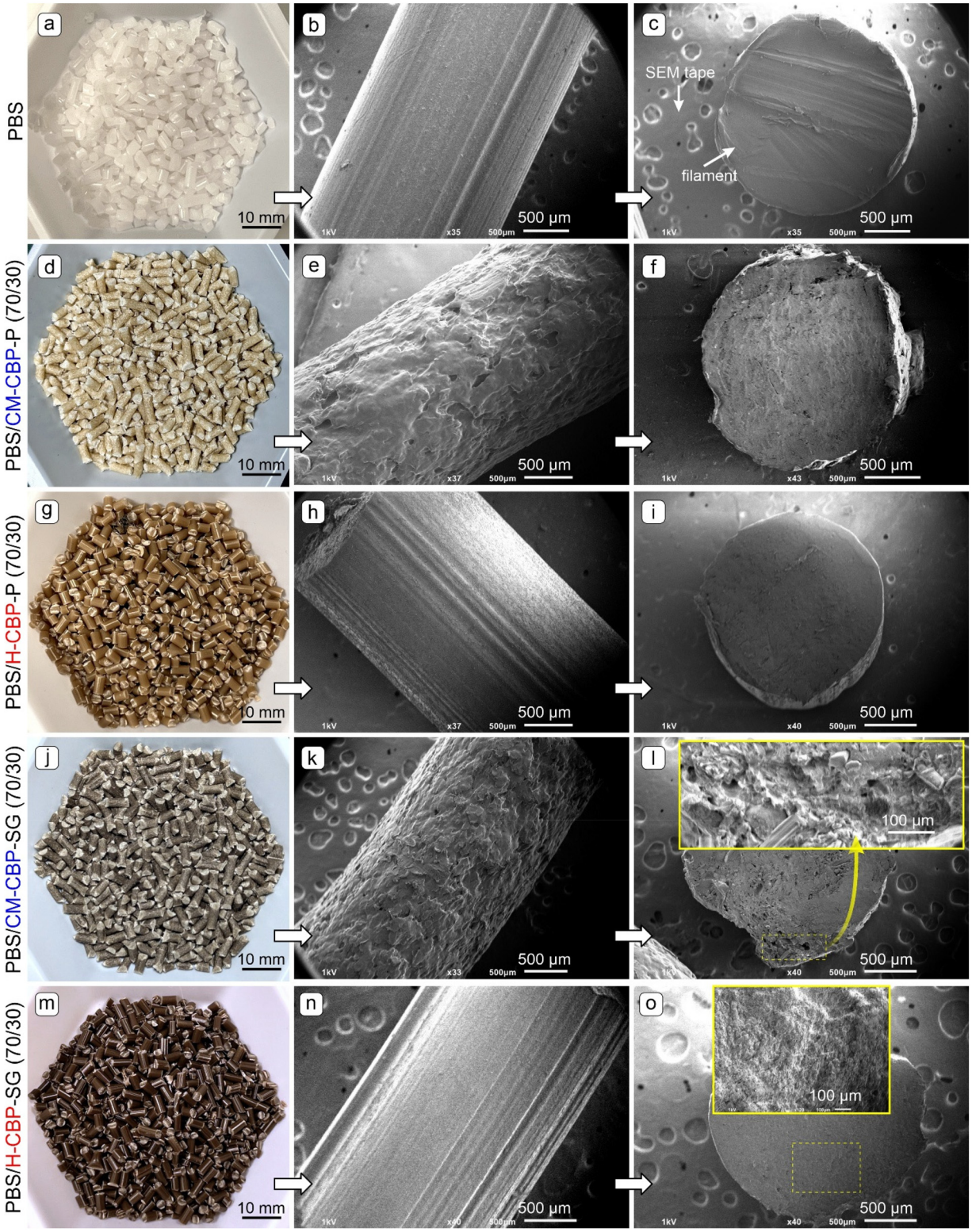

Fig. 3 Morphological comparison of PBS/CBP biocomposites prepared using cyclone milling and high-shear homogenization. (Left column) Digital photographs of neat PBS and PBS/CBP-R biocomposite filament pellets. (Middle column) Scanning electron micrographs (SEM) of the filament surfaces of neat PBS and PBS/CBP-R biocomposite filaments. (Right column) Scanning electron micrographs (SEM) of filament cross-sections of neat PBS and PBS/CBP-R biocomposites. Insets display a high-magnification view of the boxed area of the interface to highlight homogenous integration of the filler with PBS. Scale bars are shown for reference. PBS (neat PBS), PBS/CM-CBP-P (CM poplar), PBS/H-CBP-P (HSH poplar), PBS/CM-CBP-SG (CM switchgrass), PBS/H-CBP-SG (HSH switchgrass).

This journal is © The Royal Society of Chemistry 2026

Open Access Article. Published on 21 May 2026. Downloaded on 6/11/2026 11:23:03 PM.
This article is licensed under a Creative Commons Attribution 3.0 Unported Licence.

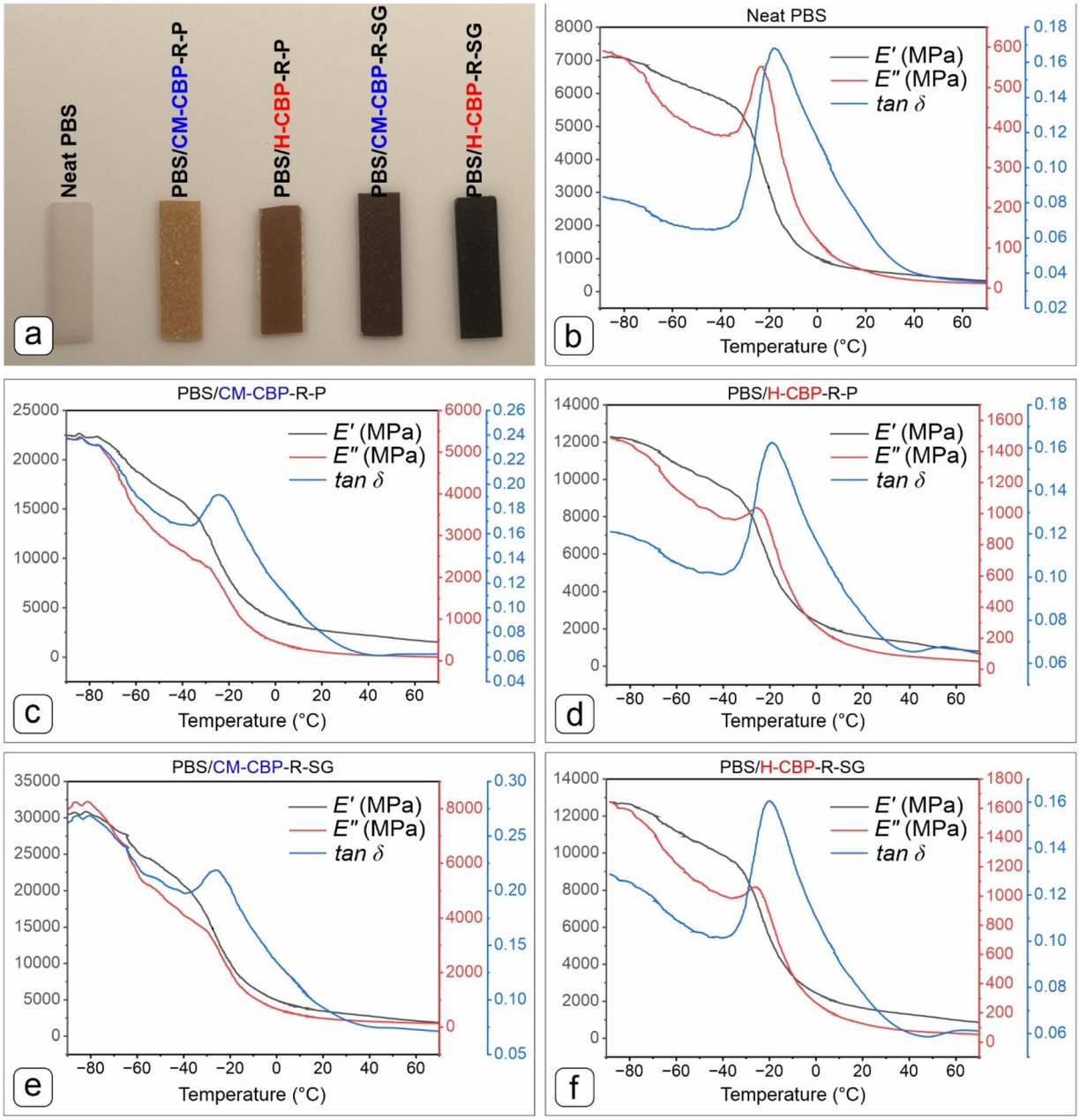

Fig. 4 Dynamic mechanical analysis (DMA) of neat PBS and PBS/CBP-R biocomposites. (a) Digital photograph of injection-molded specimens used for testing. (b–f) Thermomechanical profiles showing storage modulus (E'), loss modulus (E''), and tan δ as a function of temperature for: (b) neat PBS, (c) PBS/CM-CBP-R-P (cyclone-milled poplar), (d) PBS/H-CBP-R-P (homogenized poplar), (e) PBS/CM-CBP-R-SG (cyclone-milled switchgrass), and (f) PBS/H-CBP-R-SG (homogenized switchgrass).

the tan δ peak represents the energy dissipation (damping) of the material. Higher tan δ indicates greater molecular mobility and energy dissipation. This is often associated with weak filler–matrix interactions or increased free volume. On the other hand, low damping (*i.e.*, low tan δ) suggests restricted polymer chain mobility and stronger interfacial bonding.[75–78]

Neat PBS exhibited an initial storage modulus (E') of 7112 MPa at −90 °C and a characteristic glass transition temperature (T_g) at −17.95 °C (tan δ magnitude 0.169) (Fig. 4b). In the poplar composites, PBS/CM-CBP-R-P (Fig. 4c) showed a high initial E' of 22 633 MPa but suffers from a severe T_g depression, with the tan δ peak shifting to −24.10 °C and the E' onset occurring at −34.70 °C (high damping magnitude 0.238). These changes suggest poor interfacial adhesion and increased free volume at the LC–PBS matrix interface. Conversely, PBS/H-CBP-R-P (Fig. 4d) stabilizes the matrix with an E' of 12 221 MPa at −90 °C and maintains the T_g at −19.00 °C, while successfully anchoring polymer chains as evidenced by a suppressed tan δ magnitude of 0.163. A similar trend was observed for the switchgrass composites. PBS/CM-CBP-R-SG (Fig. 4e)

Open Access Article. Published on 21 May 2026. Downloaded on 6/11/2026 11:23:03 PM. This article is licensed under a Creative Commons Attribution 3.0 Unported Licence.

exhibited a high initial E' of 30 390 MPa, and showed a significant T_g shift to −26.05 °C and high damping (0.270), whereas the homogenized PBS/H-CBP-R-SG (Fig. 4f) restores the T_g to −19.90 °C and maintains an initial E' of 12 665 MPa. Overall, the CM samples exhibited high damping (up to 0.270), whereas the HSH-treated samples showed a suppressed tan δ magnitude of 0.163 (lower damping), which is lower than the neat PBS baseline (0.169).

Notably, the exceptionally high storage modulus (E') observed for CM samples in the glassy region (below −40 °C) is interpreted as an artifact of poor filler dispersion and direct percolation of coarse, cyclone-milled grains. In the frozen glassy state, the immobilized PBS matrix acts as a rigid medium that physically traps these large-scale heterogeneities, resulting in a high apparent stiffness. However, this phenomenon does not represent true reinforcement, as evidenced by two critical factors. First, the CM composites exhibit significant interfacial instability, characterized by a severe T_g depression and a dramatic increase in tan δ. This suggests that the large grains serve as macromolecular defects that disrupt the local packing of the PBS matrix rather than integrating with it. Second, the disparity in reinforcing efficiency becomes evident in the rubbery region (above −20 °C). As the polymer chain mobility increases, the weak CM interface fails to support effective load transfer, leading to a rapid loss of structural integrity. In contrast, HSH-refined microfibers maintained a significantly higher modulus into the rubbery state (1286 MPa at 40 °C). This represents a 156% increase over the neat PBS baseline (503 MPa) and outperforms the CM control by 21%, confirming that the HSH process facilitates a stable, integrated reinforcing network rather than a transient structural artifact.

The loss modulus (E'') profiles further support this interpretation. Neat PBS exhibited an E'' peak at −23.30 °C. For the CM-CBP-R composites, a significant downward shift in the E'' peak was observed, reaching −29.30 °C for PBS/CM-CBP-R-P and −30.70 °C for PBS/CM-CBP-R-SG. This premature energy dissipation suggests disrupted matrix packing due to the presence of CM-processed filler, which increases free volume and enhances molecular friction at lower temperatures. In contrast, the HSH-treated samples showed E'' peaks at −25.20 °C (PBS/H-CBP-R-P) and −25.60 °C (PBS/H-CBP-R-SG), closer to neat PBS. This proximity indicates that the refined microfibers do not introduce the same level of microstructural defects as the cyclone-milled bundles, instead forming a more integrated and thermally stable interface.

Based on these thermomechanical findings, a clear distinction was observed regarding the suitability of the two processing methods. Although cyclone milling produced rigid fillers, the resulting composites suffer from microstructural instability and poor interfacial bonding, rendering them unsuitable for reliable high-performance applications. Consequently, CM-processed samples were excluded from further investigation. The subsequent sections detailing thermal characterization (TGA, DSC, MFR) and tensile properties focus exclusively on HSH-refined biocomposites to establish their performance profile and demonstrate their viability for structural 3D printing applications.

3.4. Thermal characterization of biocomposites

A comprehensive understanding of the thermal behavior of both neat PBS and its biocomposites with HSH-processed switchgrass and poplar CBP-R is crucial for assessing their processability and performance. This was achieved through thermogravimetric analysis (TGA), differential scanning calorimetry (DSC) and melt flow rate (MFR) studies (Fig. 5). TGA revealed distinct thermal degradation profiles for PBS, raw biomass materials, and their composites under different processing conditions. Pure PBS exhibits a single major degradation event with an onset temperature at 300 °C, a maximum degradation temperature at 395 °C, and a sharp weight loss between 350–420 °C, corresponding to its primary decomposition phase. Negligible char residue remains beyond 450 °C, indicating complete degradation.

Analysis of switchgrass and poplar H-CBP-R showed that both raw feedstocks exhibit multi-step thermal degradation behaviors (Fig. 5a-DTG). TGA and DTG profiles of H-CBP-R-P show a 4-step degradation profile (Fig. 5a), where the initial weight loss below 100 °C is attributed to the evaporation of physically adsorbed moisture. This is followed by a second mild degradation at 150–210 °C (volatile species), a third significant degradation stage occurring between 200–300 °C with intense degradation at 275 °C, and finally at 450 °C. Similarly, TGA and DTG data of H-CBP-R-SG (Fig. 5a) shows a two-step thermal degradation behavior, initiated by the same initial weight loss below 100 °C attributed to the evaporation of physically adsorbed moisture, followed by a second significant degradation event from 170–390 °C with intense degradation at 330 °C. Beyond 500 °C, both H-CBP-R samples exhibit slow weight loss due to the decomposition of highly condensed carbon structures, leaving char residues. As shown previously,[79] raw biomass (H-CBP-R-SG and CBP-R-P) typically shows hemicellulose degradation between 200–300 °C. Hemicellulose is an amorphous heteropolysaccharide and possesses the lowest thermal stability among the three main lignocellulosic components. Its degradation involves the breakdown of oxygen-containing functional groups, resulting in a maximum degradation temperature around 275 °C, that is often observed as a pronounced peak or shoulder in the DTG curve.[79,80] Cellulose is more thermally stable than hemicellulose and thus undergoes its primary thermal degradation at higher temperatures (290–400 °C) with an intense peak near 350 °C. Lignin degrades over a broader temperature range, extending up to 900 °C, contributing to char residue formation at high temperatures.[81,82] The observed enhancement in the thermal stability of lignocellulosic fillers within the PBS matrix indicates beneficial interactions within the composite. We hypothesize that improved dispersion and interactions at the PBS–LC fibers interface can reduce the mobility of biomass constituents,[13,20,83] thereby reinforcing their thermal resistance.[84] Studies have shown that enhanced interfacial bonding, sometimes achieved through surface modifications

 This journal is © The Royal Society of Chemistry 2026

Open Access Article. Published on 21 May 2026. Downloaded on 6/11/2026 11:23:03 PM.
This article is licensed under a Creative Commons Attribution 3.0 Unported Licence.

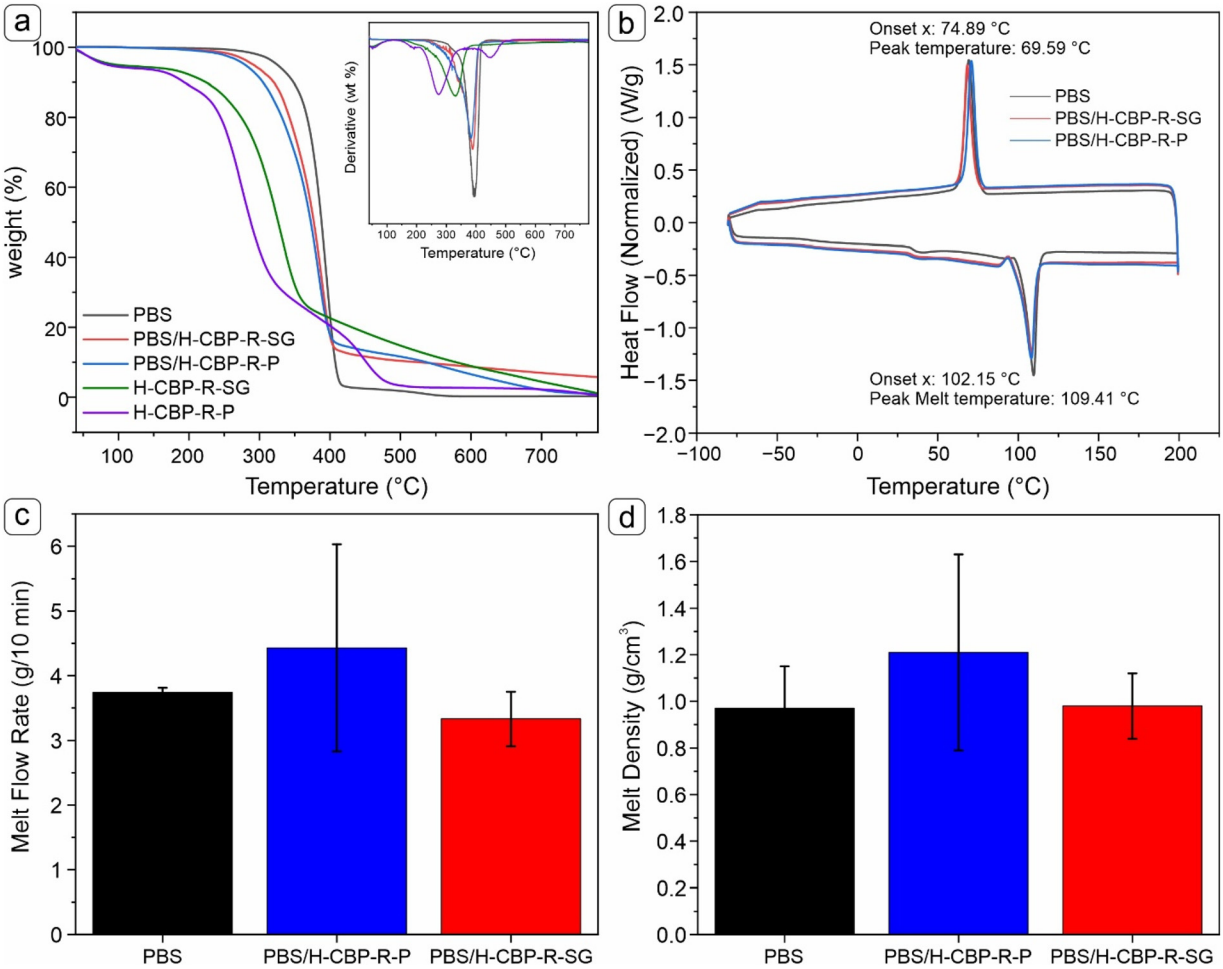

Fig. 5 Thermal characterization of PBS and H-CBP-R composites. (a) Thermogravimetry Analysis (TGA); (b) differential scanning calorimetry (DSC); (c) melt flow rate analysis, data is represented as the average ± S.D. of three technical replicates (n = 3) and (d) melt density analysis of PBS in comparison with PBS-based CBP-R composites, data is represented as the average ± S.D. of three technical replicates (n = 3). Inclusion of H-CBP-R residues maintains the core thermal stability of the PBS matrix while significantly reducing the melt flow rate, indicating that the microfibers provide a structural network that enhances melt viscosity, a critical factor for successful 3D printing and filament deposition.

of lignocellulosic fillers or the use of compatibilizers, leads to increased thermal degradation resistance.[85] These potential chemical interactions can stabilize labile groups and facilitate cross-linking reactions, which contribute to higher char yields and elevated degradation onset temperatures.[86]

Differential scanning calorimetry (DSC) was employed to further elucidate the thermal transitions and phase behavior of the materials (Fig. 5b). Neat PBS exhibited distinct and well-defined melting (T_m), and crystallization (T_c) temperatures, which are characteristic features of a semi-crystalline polymer.[87] The DSC thermograms revealed that pure PBS typically melts in the range of 110–115 °C and crystallizes near 80 °C. The addition of H-CBP-R did not affect the crystallization temperatures (Fig. 5b).

MFR measurements conducted at 190 °C, showed values of 3.74, 4.43, and 3.33 g per 10 min for PBS, PBS/H-CBP-R-P, and PBS/H-CBP-R-SG, respectively (Fig. 5c and d). Despite slight variations, all measured MFR values remained within the processable range for PBS, making them suitable for injection molding. It is important to consider that MFR analysis conducted at elevated temperatures can induce biomass caramelization, potentially affecting the measured flow properties. Fig. 5d shows the corresponding melt densities of 0.97, 1.21, and 0.98 g cm^{-3} for PBS, PBS/H-CBP-R-P, and PBS/H-CBP-SG, respectively.

3.5. Mechanical performance

A detailed tensile and impact strength analysis was conducted to evaluate the mechanical performance of biocomposites formulated with HSH-treated CBP-R. The tensile properties of dogbone specimens were assessed using a Shimadzu Autograph AGS-X universal testing machine (Fig. 6a and b). The neat PBS served as the baseline, demonstrating a Young's modulus of 0.36 ± 0.02 GPa, a high strain at break of 236 ± 60%, a stress at break of 39 ± 6 MPa, and a yield strength of 17.6 ± 0.4 MPa, which is characteristic of a ductile polymer

Open Access Article. Published on 21 May 2026. Downloaded on 6/11/2026 11:23:03 PM.
This article is licensed under a Creative Commons Attribution 3.0 Unported Licence.

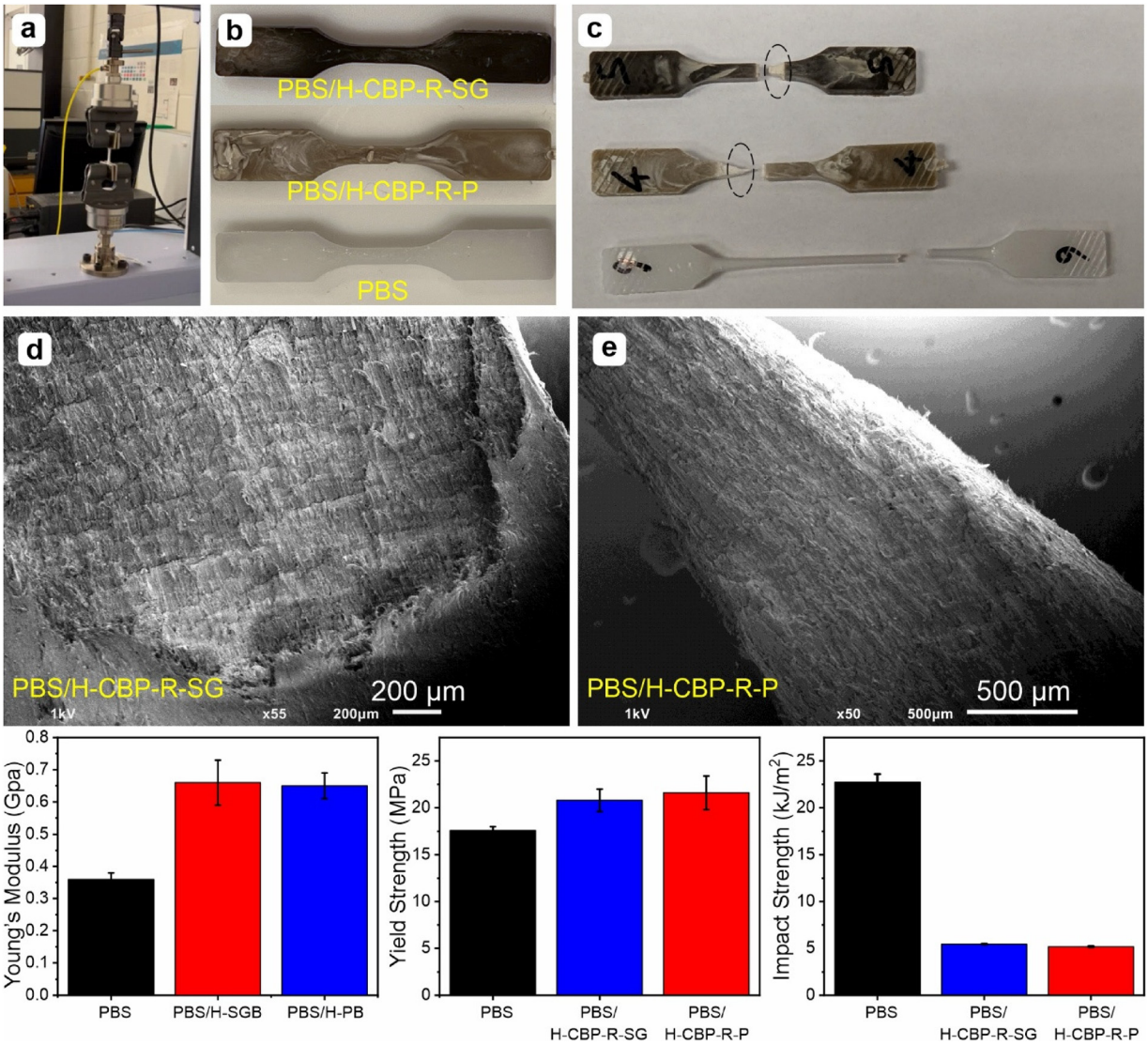

Fig. 6 Mechanical tensile testing of PBS and H-CBP-R biocomposites. (a) Shimadzu tensile testing unit used for uniaxial tensile and impact testing of injection-molded specimens; (b) injection-molded dog-bone specimens before testing showing PBS (bottom), PBS/H-CBP-R-P (middle) and PBS/H-CBP-R-SG (top); (c) representative dog-bones after tensile failure with fracture locations indicated by dashed circles; (d) SEM micrograph of the cross-section of a fractured PBS/H-CBP-R-SG dog-bone showing interfacial features; (e) SEM micrograph of the fractured PBS/H-CBP-R-P dog-bone tip showing fracture topography. Tensile and impact mechanical properties of neat PBS and composite formulations presented as bar graphs: (f) Young's modulus demonstrating a marked stiffness increase for PBS/H-CBP-R-SG and PBS/H-CBP-R-P compared with neat PBS; (g) yield strength showing moderate improvement for composites relative to PBS; (h) impact strength indicating a substantial decrease in impact resistance for both composite formulations *versus* neat PBS. Error bars represent standard deviation from at least five independent specimens. Measurements were done in triplicates and average values are reported.

capable of significant deformation before fracture. In contrast, the incorporation of H-CBP residuals significantly altered the mechanical properties of both composite formulations. For the PBS/H-CBP-R-SG and PBS/H-CBP-R-P composites, the Young's modulus nearly doubled to 0.66 ± 0.07, and 0.65 ± 0.04 GPa, respectively (Fig. 6f and g), indicating a substantial increase in stiffness compared to neat PBS. This enhancement in stiffness is typical for polymer composites containing a rigid filler.[88] To contextualize these mechanical improvements within the broader materials landscape, a Young's modulus *versus* tensile strength Ashby plot was generated (Fig. 7 and Tables S3 and S4). As shown in the property map, the incorporation of H-CBP residuals shifts the application scope of the materials from the flexible commodity packaging regime, typical of neat PBS and LDPE, into the general engineering and consumer goods' quadrant. While the biocomposites exhibit reduced ductility, they occupy a performance space that bridges the gap between flexible biopolymers and rigid engineering plastics. Specifically, the H-CBP-R composites achieve a stiffness-to-strength ratio comparable to unrein-

Open Access Article. Published on 21 May 2026. Downloaded on 6/11/2026 11:23:03 PM.
This article is licensed under a Creative Commons Attribution 3.0 Unported Licence.

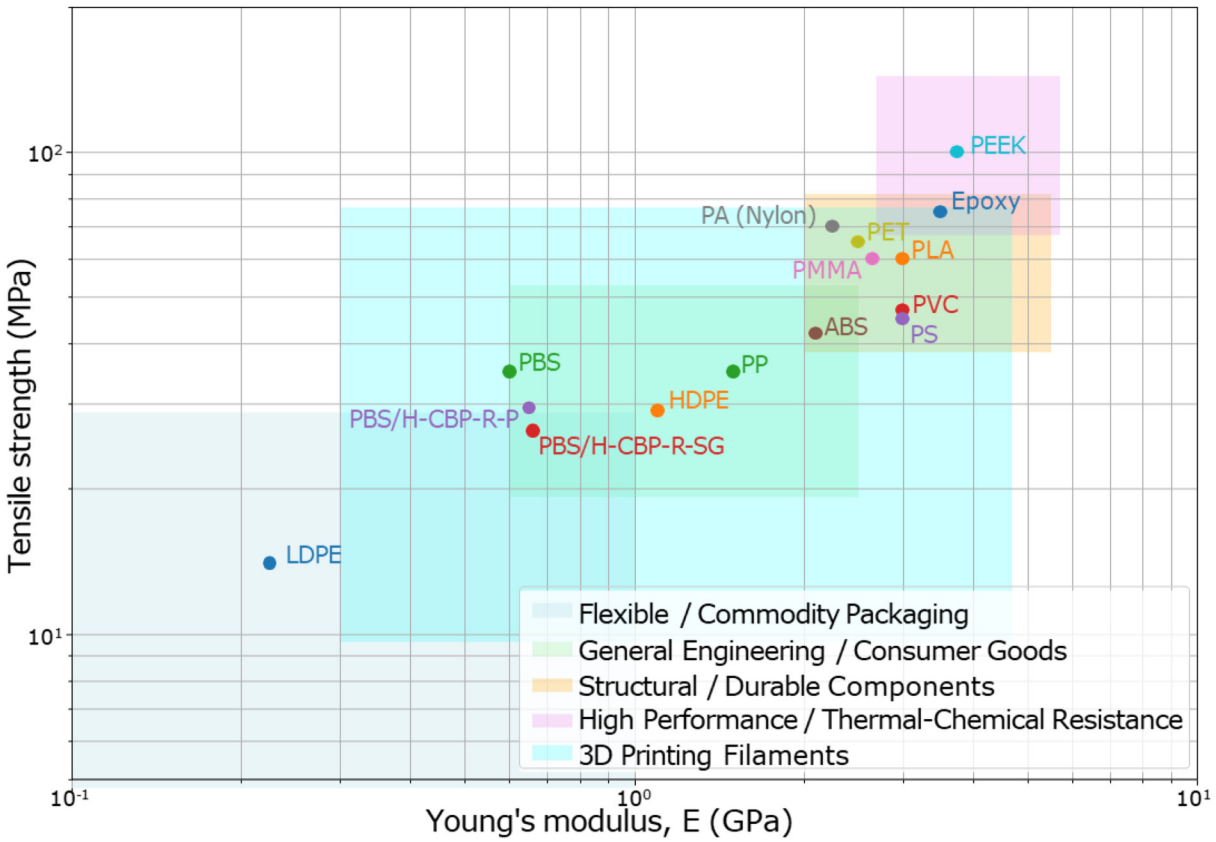

Fig. 7 Ashby mechanical property map of tensile strength *versus* Young's modulus. The plot benchmarks PBS/H-CBP-R-SG and PBS/H-CBP-R-P biocomposites against common fossil-based plastics (LDPE, HDPE, PP, PET) and bio-based incumbents (PLA, PBS). The shaded regions indicate typical application envelopes, demonstrating the transition of the HSH-refined composites from flexible packaging performance to the general engineering and structural components regime.

forced Polypropylene (PP) and High-Density Polyethylene (HDPE), validating their potential as sustainable alternatives to fossil-derived structural plastics. However, this increase in stiffness came at a notable trade-off in ductility, evident from the decrease in the strain at break to 12.3 ± 3% and 12.5 ± 2% in PBS/H-CBP-R-SG and PBS/H-CBP-R-P, respectively. This drastic reduction in ductility suggests a transition to more brittle failure. While the stress at break showed a reduction for both composites compared to neat PBS (26.4 ± 1.1 MPa for PBS/H-CBP-R-SG and 29.4 ± 0.8 MPa for PBS/H-CBP-R-P), the increase in yield strength to 20.8 ± 1.2 MPa and 21.6 ± 1.8 MPa, respectively, indicates that the composites can withstand higher stresses before permanent deformation begins, aligning with their increased stiffness.

The observed "cone" patterns (Fig. 6c) after tensile failure for both composites were noteworthy and provide critical insights into their fracture mechanisms. While a typical ductile cup-and-cone fracture is characterized by significant necking and substantial plastic deformation, the biocomposites exhibited low strain at break and no obvious necking prior to failure. The observed cone pattern, therefore, is more indicative of internal delamination during the fracture process. This phenomenon is likely a result of changes in stress distribution within the matrix due to the high filler loading. To investigate this further, the fractured surfaces were examined by scanning electron microscopy (SEM) (Fig. 6d and e). Our data showed that the composites exhibited relatively smooth fracture surfaces, characterized by hackle marks and minimal evidence of plastic deformation, further corroborating a brittle failure mode.[89] These microscopic features align with the macroscopic observation of low strain at break, suggesting that the increased stiffness imparted by the LC phase is accompanied by localized debonding between the filler and matrix. This promotes brittle crack propagation and reduces the capacity of the composite for plastic energy dissipation.

Higher impact strength is particularly favorable for applications where materials are subjected to sudden loads or impacts. Thus, in order to further pinpoint the best-suited applications for the prepared composites, we measured their notched Izod impact strength (Fig. 6h). A substantial decrease in impact resistance was observed for both H-CBP-R based composite formulations compared to neat PBS (Fig. 6h). The observed reduction in impact strength of the biocomposites is a direct consequence of the microstructural changes induced by incorporation of H-CBP residuals. During testing, the stiffer

Open Access Article. Published on 21 May 2026. Downloaded on 6/11/2026 11:23:03 PM. This article is licensed under a Creative Commons Attribution 3.0 Unported Licence.

structure formed by the LC fibers resists deformation around the notch. However, unlike ductile materials that can absorb impact energy through extensive plastic deformation and crack blunting,[90] these stiffer composites tend to localize the applied force at the notch tip. This localization, combined with the matrix's reduced ability to dissipate energy, leads to an abrupt failure and brittle crack propagation.

The observed mechanical trade-offs, specifically by increased Young's modulus and reduced impact resistance, define a specific application centered on structural rigidity, where rigidity and structural integrity under static loading are prioritized. This includes precision manufacturing and 3D printing. Although neat PBS is highly ductile, incorporation of 30 wt% H-CBP-R transforms the material into a stiffness-dominated composite comparable to certain grades of Polypropylene (PP) and Bio-Polyethylene (see benchmarking in Table S4, SI). Therefore, these biocomposites are less suitable for high-impact applications but provide the necessary mechanical stability for precision manufacturing. However, to fully justify the HSH processing step and to evaluate molecular adhesion between the phases, a deeper investigation into the thermomechanical and viscoelastic behavior is required.

3.6. Biodegradability and environmental disintegration

The end-of-life behavior of the biocomposites was evaluated through composting studies conducted under real-world garden conditions over 6 months to assess environmental persistence. Unlike laboratory-controlled settings with optimized, constant higher temperatures, these garden conditions in a greenhouse-enclosed composter (Fig. S1a) expose the materials to natural thermal fluctuations and indigenous soil microbiota. In such environments, biodegradation is initiated by moisture absorption from the surrounding soil, which serves as a precursor to microbial colonization and enzymatic breakdown. The internal temperature of a garden greenhouse composter typically follows a dynamic profile. During the initial active phase, microbial metabolism generates heat, often maintaining internal temperatures between 25 °C and 35 °C, which can occasionally spike higher depending on the organic load and solar gain within the greenhouse. As the process matures, the temperature settles toward the ambient greenhouse average, typically ranging from 18 °C to 25 °C.[91,92] This fluctuating temperature profile is critical as it facilitates the transition from mesophilic bacterial activity to fungal degradation, both of which contribute to the structural breakdown of the PBS matrix.

Quantitative monitoring of sample weights (Fig. S1g) distinguished the initial moisture uptake and subsequent mass loss during soil incubation. PBS/H-CBP-R-SG showed greater sensitivity than neat PBS, evidenced by a 5.8 wt% increase in weight, from 998.1 to 1056.0 mg, in the first 11 days, compared to only 1.5% for neat PBS. This higher moisture uptake reflects the hydrophilic nature of the refined biomass microfibers, which facilitate water penetration into the composite structure. After saturation, the samples exhibited distinct degradation behavior. Over 6 months, PBS/H-CBP-R-SG samples underwent substantial disintegration, resulting in a final dry weight of 960.0 mg. This represents a total mass loss of nearly 100 mg from its peak wet weight, indicating that the material is being deconstructed. Conversely, neat PBS remained remarkably stable, with a final weight of 871.0 mg, showing almost no mass loss from its peak wet weight.

The initial injection-molded specimens for both neat PBS (Fig. 8a) and PBS/H-CBP-R-SG (Fig. 8c) show smooth surfaces. After 6 months in the garden composter, however, the morphological changes are profound. While the neat PBS (Fig. 8b) shows only minor surface dulling, the PBS/H-CBP-R-SG specimen (Fig. 8d) exhibits extreme fragmentation and a characteristic porous texture. These observations align with the thermomechanical findings in section 3.3, the homogenized microfibers that provided mechanical reinforcement during the material's usage for intended applications also facilitate a rapid return to the environment during its end-of-life phase under natural composting conditions.

3.7. 3D printing applications and filament performance

The adaptability and potential of these biocomposites in advanced additive manufacturing techniques were rigorously assessed through comprehensive 3D printing tests, demonstrating their practical applicability. The results, as shown in Fig. 9, highlight an advantageous contrast in 3D printing performance between neat PBS and its biocomposite counterparts. This transition from injection-molded specimens to fused deposition modeling (FDM) filaments is a necessary step in validating these materials for decentralized, low-waste manufacturing.

Neat PBS pellets, specifically injection molding grade FZ71 as shown in Fig. 9a, served as the baseline for filament production. The resulting 1.75 mm diameter filament (Fig. 9b) was used in 3D printing trials conducted with a BambuLab A1 mini and Prusa Research Mk3s with 0.6 mm nozzle, 95 °C bed temperature, and 180 °C nozzle temperature. The thermal challenges observed during these trials correlate directly with the thermomechanical profiles established in section 3.3. Neat PBS exhibited problematic shrinkage during the cooling phase (Fig. 9c), resulting in severe delamination from the print bed, even at an elevated bed temperature. The DMA data provides a molecular explanation for this failure, as the high segmental mobility of neat PBS polymer chains, near its T_g, enables rapid crystalline reorganization and significant volume contraction upon cooling. We hypothesize that without the reinforcing LC microfibers to anchor these chains, the internal stresses generated during the layer-by-layer cooling process exceed the adhesive forces of the print bed. Such severe warpage makes neat PBS challenging for reliable 3D printing without specialized, high-temperature chambers. Furthermore, the low storage modulus E' of neat PBS in the rubbery region, as seen in the DMA analysis, suggests that the printed layers lack the structural stiffness required to resist the pulling forces of cooling-induced shrinkage, leading to the observed part failure.

In contrast, the PBS/H-CBP-R-SG and PBS/H-CBP-R-P biocomposite filaments (Fig. 9e and h) demonstrated significantly

 This journal is © The Royal Society of Chemistry 2026

Open Access Article. Published on 21 May 2026. Downloaded on 6/11/2026 11:23:03 PM.
This article is licensed under a Creative Commons Attribution 3.0 Unported Licence.

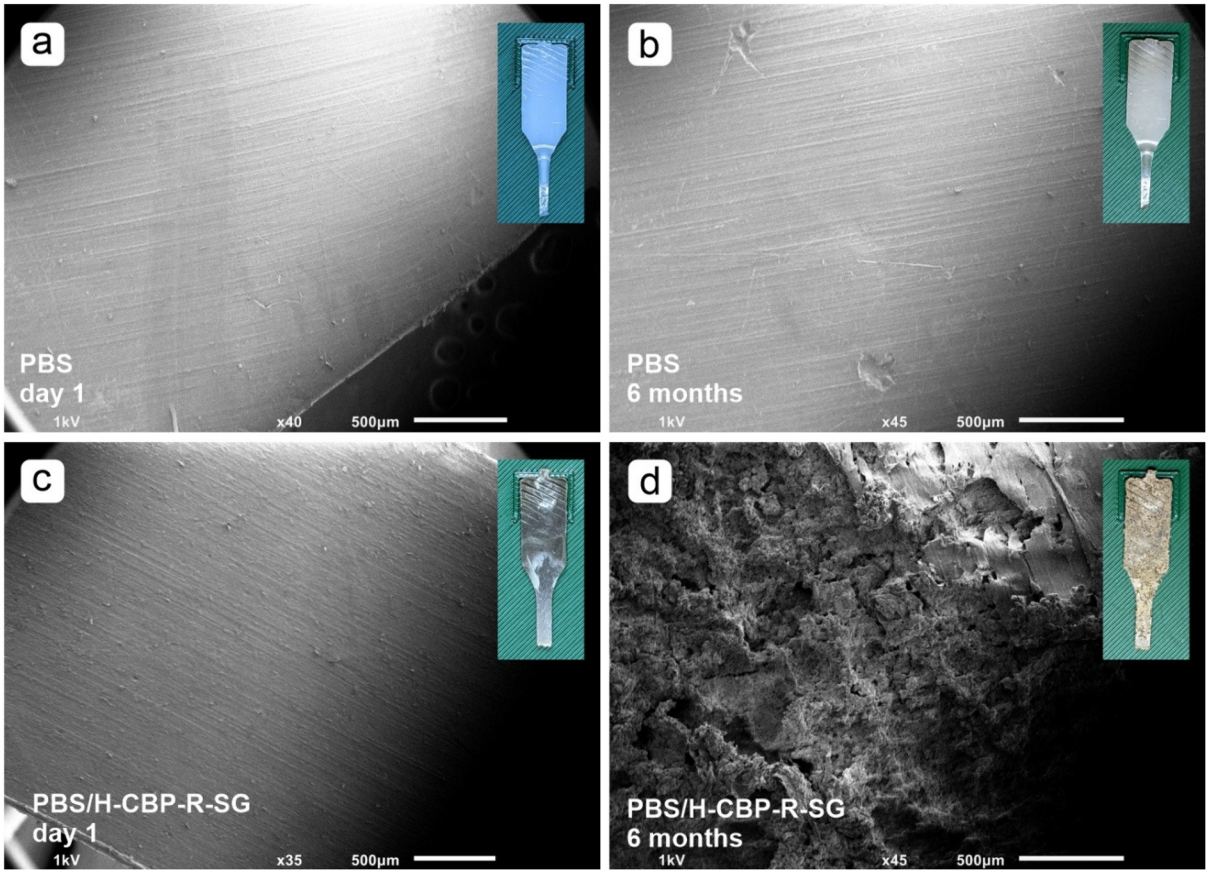

Fig. 8 Visual assessment of environmental disintegration *via* composting. Comparison of injection-molded neat PBS dog bone specimens (a) before and (b) after 6 months of composting, showing minor surface dulling and pitting. (c) PBS/H-CBP-R-SG biocomposite (70/30 wt%) before composting and (d) after 6 months of exposure, exhibiting extreme fragmentation, extensive surface erosion, and a characteristic porous architecture resulting from accelerated microbial degradation and moisture-induced swelling of the refined microfibers in a natural environment.

improved 3D printability and dimensional stability. The inclusion of 30% LC biomass microfibers acted as an internal structural scaffold, effectively countering the thermal contraction characteristic of neat PBS. The observed improvements in filament thermal processability and dimensional stability resulting from filler incorporation, has been previously reported for biomass-based composites, but requires additives and compatibilizers.[93–95] This stabilization of our composites is directly supported by the DMA results, which showed a 152% increase in the storage modulus E' in the rubbery region. During the FDM process, as the molten filament leaves the nozzle and begins to cool, this drastically higher stiffness allows the composite to resist the internal stresses that typically cause warping and delamination in neat PBS. Furthermore, the suppression of the tan δ peak magnitude in the biocomposites confirms that the HSH-refined microfibers significantly restrict the segmental mobility of the PBS polymer chains. In 3D printing, this molecular anchoring minimizes the dramatic volumetric shrinkage associated with the crystallization of the PBS matrix. Consequently, the biocomposites exhibited high interlayer and bed adhesion, leading to high-quality printed objects (Fig. 9f and i) with precision comparable to industry-standard polylactic acid (PLA). This precision is not merely a result of improved processing but reflects a fundamental shift in the material's mechanical classification. As shown in the Ashby property map (Fig. 7), while neat PBS resides in the flexible commodity packaging regime, the H-CBP-R biocomposites migrate into the general engineering and 3D printing filament quadrant. By bridging the property gap between neat PBS and higher-modulus incumbents like PET and PLA, these composites offer the structural rigidity required for high-fidelity additive manufacturing while maintaining the sustainable advantages of a bio-derived system. The ability to use standard PLA profiles (180 °C nozzle, 0.2 mm layer height) without extensive equipment modification further highlights the commercial viability of these valorized residues.

Beyond thermal stability, a noteworthy advantage was the superior ambient stability of the PBS/H-CBP-R filaments. While many bio-based filaments like PLA are inherently hygroscopic and become brittle over time due to moisture-induced chain scission, the PBS/H-CBP-R filaments remain ductile and printable even after multiple months of ambient exposure, consistent with the moisture absorption data. Although the

Open Access Article. Published on 21 May 2026. Downloaded on 6/11/2026 11:23:03 PM.
This article is licensed under a Creative Commons Attribution 3.0 Unported Licence.

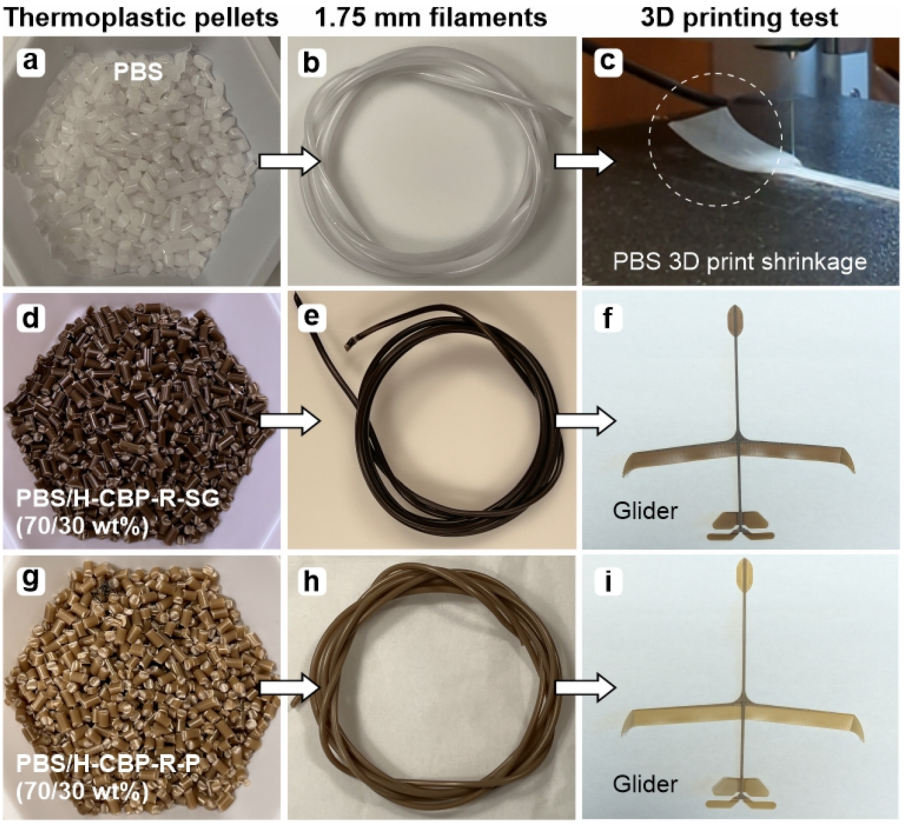

Fig. 9 3D-printing performance of neat PBS and PBS/biomass biocomposites. (a) PBS FZ71 injection molding grade pellets, the starting material for neat PBS filaments. (b) A 1.75 mm diameter filament extruded from neat PBS pellets. (c) 3D printing test results with neat PBS. Shrinkage/warping occurred during printing leading to delamination of the part from the print bed surface after the second layer, even at an elevated bed temperature of 95 °C. (d) PBS/H-CBP-R-SG biocomposite pellets and (e) a 1.75 mm diameter filament formulated at a 70/30 weight percentage. (f) Successful 3D printing test using the PBS-switchgrass biocomposite, demonstrating drastically improved printability. (g) PBS/H-CBP-R-P biocomposite pellets and (h) 1.75 mm diameter filament formulated at a 70/30 weight percentage. (i) 3D printing test using the PBS-poplar biocomposite. The inclusion of H-CBP-R microfibers provides a critical increase in melt stability and structural stiffness, which effectively counteracts the high thermal shrinkage of neat PBS and enables the high-fidelity 3D printing of complex geometries.

CBP-R fillers are hydrophilic, the high interfacial integrity between the homogenized microfibers and the PBS matrix likely prevents the wicking of moisture into the core of the filament. This enhanced shelf-life reduces material waste and increases the practical appeal of these composites for distributed manufacturing, in situations where climate-controlled storage is unavailable. Further, the distinct mechanical profile of the PBS/H-CBP-R biocomposites characterized by a near-doubling of the Young's modulus and a concomitant reduction in impact resistance dictates a specific application envelope centered on dimensional stability and structural rigidity. These materials are ideally suited for FDM 3D printing as demonstrated in the current study, where the increased stiffness effectively counteracts the thermal shrinkage and warping common in neat PBS, enabling the production of high-fidelity, complex geometries. In addition, they are well-positioned for static structural components, such as interior architectural elements, lightweight frames, and housings for consumer electronics, where resistance to deformation under constant load is a primary requirement. Conversely, the transition to a brittle failure mode renders these composites explicitly unsuitable for high-impact environments, such as automotive safety components, or applications requiring repetitive flexing, such as living hinges. Taken together, our data suggest that H-CBP-R biocomposites may serve as sustainable replacements for rigid thermoplastics like polypropylene (PP) in static, non-dynamic use cases (Fig. 7).

3.8. Techno-economic analysis (TEA)

To explore the economic potential for blending lignin-rich residuals with bioplastics, we performed process modeling and (TEA for biocomposite production. We chose to analyze the scenario where solid residuals from an ethanol-producing CBP biorefinery are sold as a co-product to the biomaterial production facility. Although the biomaterial production could theoretically be included inside the battery limits of the CBP biorefinery, this would make the CBP biorefinery economics contingent upon the consistent sale of the composite. Selling the residual directly as a co-product offers flexibility since the rest of the residuals are still burned in the boiler to produce heat and electricity. This framework also allows us to independently analyze the benefits to the CBP biorefinery for selling

This journal is © The Royal Society of Chemistry 2026

Open Access Article. Published on 21 May 2026. Downloaded on 6/11/2026 11:23:03 PM.
This article is licensed under a Creative Commons Attribution 3.0 Unported Licence.

the residuals as a co-product as well as the influence of co-product price on both facilities.[96]

We first developed a process model for CBP similar to previous published works (Fig. 10).[59] The model is described here in brief, but a more thorough description is provided in the SI. The biomass substrate is first mechanically refined to reduce the particle size and increase solubilization efficiency. The mechanical refining process was modeled based on the work from Davis *et al.*[97] includes disc refining and a roller mill. After size reduction, the processed biomass is loaded into 1 MM gallon fermenters at 20 wt% solids loading along with seed inoculum of thermophilic bacteria. Solubilization and fermentation occur over the course of five days, reaching 90% solubilization and 88% conversion of solubilized glucose to ethanol, representing a net ethanol yield of 80% of theoretical (0.41 g ethanol per g glucans + g xylan). Minor hemicellulose sugars such as mannose, galactose, and arabinose were considered non-fermentable. After fermentation, the broth (91 wt% water) contains the ethanol product (2.8 wt%) as well as the residual solids which contains the cell mass as well as carbohydrates and lignin in the pulp (2.6 wt%) which was not converted in fermentation. The ethanol is purified *via* distillation and molecular sieves using the configuration described by Humbird *et al.*,[58] producing a 99.3 wt% ethanol product. Residual solids from fermentation are contained in the bottom product of the first distillation columns and dried to 35 wt% moisture content in a lignin filter press.

The CBP biorefinery processes 2000 dry tonnes of poplar biomass per day, producing 40.5 MMGGE (million gallons of gasoline equivalent; 186 kt ethanol per year) of ethanol fuel assuming 7884 operational hours per year (90% stream factor). Approximately 170 dry kt per year of residuals (35 wt% moisture; 259 wet kt per year) are also produced in the process. In the base case, this lignin-rich CBP residual is burned in a high solids boiler along with biogas produced from on-site wastewater treatment to generate heat and electricity, similar to previous analyses.[58] This fully supplies the heat (64.8 Gcal h^{-1}) and electricity (29.2 MW) needed for the biorefinery, and produces excess electricity (16.9 MW) which is sold to the grid. The minimum ethanol selling price (MESP) was $3.52 per GGE, driven mostly by biomass feedstock, glucose for seed production, as well as the capital expenses. Electricity sales offset $0.19 per GGE.

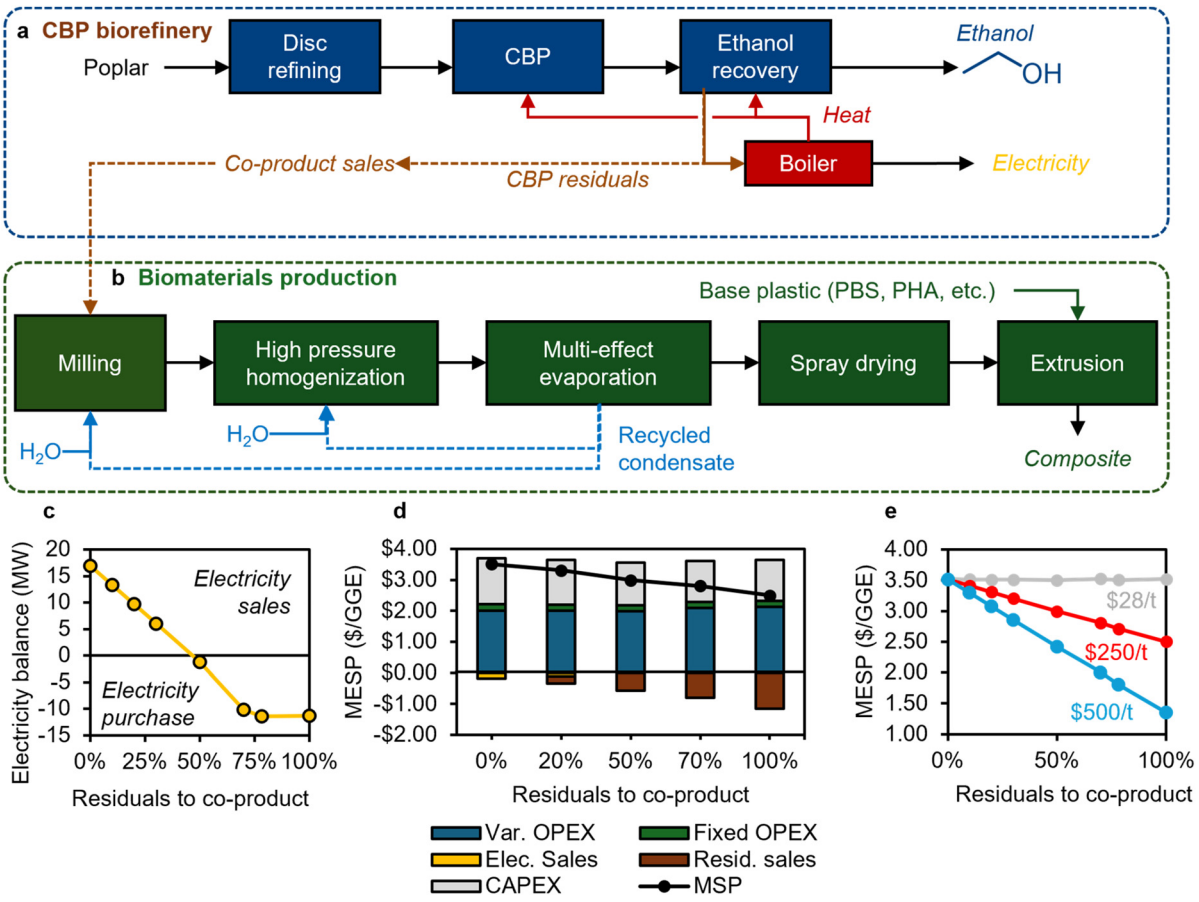

Fig. 10 Techno-economic impact of selling residuals obtained in an integrated poplar biorefinery. (a) Prodiction scheme of a CBP refinery producing ethanol and CBP residuals, which can be burned onsite to produce heat/electricity or sold as a co-product. (b) Biomaterials production scheme. (c) Electricity balance of the plant *versus* the percentage of the residuals flow diverted to co-product sales instead of burning for electricity production. (d) MESP breakdown showing the decrease in MESP with increasing amount of residuals diverted to co-products (e) Impact of CBP residuals selling price on the MESP.

Open Access Article. Published on 21 May 2026. Downloaded on 6/11/2026 11:23:03 PM. This article is licensed under a Creative Commons Attribution 3.0 Unported Licence.

Although lignin burning is common in biorefinery designs, the heat and electricity generated are considered low-value co-products. Kubis and Lynd recently demonstrated that selling all the residuals as co-product fuel pellets ($166 per ton) increased revenues and ultimately reduced the MESP.[96] We first analyzed the impact of diverting CBP residuals to be sold as a co-product. Diverting the residuals from the boiler has several effects on the CBP biorefinery. As the amount of residuals diverted for co-product sales increases, the amount of electricity generated onsite (as well as the size of the boiler) decreases. When more than 47% of the residuals (79 kt per year) are diverted for sale, the CBP biorefinery no longer produces excess electricity and must purchase electricity from the grid to meet power needs (Fig. 10c). The biorefinery can still produce sufficient heat from biogas/sludge (produced onsite from wastewater treatment) combustion past this point, but must supplement with purchased natural gas when more than 78% of the residuals are sold to the market.

The economic impact of residuals diversion depends on the sale price of the co-product. The price of the residual co-product was first varied to find the breakeven point where selling residuals provided no change to the MESP. Residuals need to be sold above $28 per dry tonne to offset the lost revenues from electricity sales. Above this price, residual sales provide a net reduction to MESP (Fig. 10d and e). If residuals are sold at $250 per dry tonne, the MESP can be lowered by up to 29% to $2.50 for the case of 100% diversion to co-product sales. Part of this MESP reduction is due to the decrease in the boiler size (steam flow rate decreased from 267 tonne per h when all residuals are burned to 149 tonne per h when all residuals are sold), which reduced the installed cost of the boiler process area from $93MM to $61MM.

Although the complete diversion of CBP residuals to co-product sales lowered MESP by the greatest amount, there may be limiting constraints on the amount of residuals which can be sold depending on the application of such material. Established markets such as biomass fuel pellets used by Kubis and Lynd[96] may be able to accept a large influx of supply without seeing oversupply or price decreases. However, in the current case of selling biomaterials, the annual dry residuals flowrate (170 kt per year) exceeds the capacity of some current bioplastic production facilities[98] even prior to considering the plastic for blending. A notional biomaterial production facility which processes 100% of the residuals of the CBP biorefinery into a 30 wt% blend would have an annual capacity of ~624 kt per year, which greatly exceeds the current scale of PBS production (~90 kt per year)[99] and is in the range of large polyethylene production facilities.[100] Thus, complete diversion of the CBP residuals to a single biomaterial production facility may be infeasible or at best represents a future case with more established economics and risks. A single CBP biorefinery may be able to sell residuals to multiple outlets, however there may exist similar limitations of the market size for those products. Given these considerations, we set the scale of the composite production facility to 58 kt per year (nameplate capacity), in the range of some recent bioplastic facilities, and adjusted the flow rate of diverted CBP residuals accordingly. Assuming a 30 wt% blend of residual with bioplastic, the CBP refinery can sell ~10% of the residual flow to the biomaterials production facility. The CBP biorefinery still produces 13.5 MW of excess electricity which is sold to the grid. Together, the MESP is reduced to $3.41 per GGE.

In the biocomposite facility (Fig. 10b), the dried residuals are first mixed with additional water to reduce the solids content to 30 wt% solids and fed to a disc refiner/roller mill to reduce particle size, based on the recent work from Davis *et al.*[97] The amount of milling required here will depend on the initial milled size when entering the CBP biorefinery, as well as the CBP conditions which affect biomass solubilization, however here it was assumed that the dry solids required 0.2 kWh kg^{-1} of electricity to reduce the particle size to below 200 μm particle size, similar to what was achieved in the lab *via* cyclone milling. Additional water is then added to bring the solids content down to 2 wt% solids content prior to homogenization. Costs and operating parameters for homogenization were taken from a recent report on algae biomass processing.[101] Power consumption in homogenization was calculated by scaling the power from that work (0.44 kWh per kg dry) biomass by the dry solids content (10 wt% in Davis *et al.* and 2 wt% in the base case of this work). After homogenization, the solution is concentrated to 50 wt% solids using multi-effect evaporation with mechanical vapor compression.[102] The mixture is then further dried to 5 wt% water in a spray drier. The dried solid is then mixed with the bioplastic in an extruder to produce the final composite product.

Fig. 11 presents the economic results for the composite production process. Here, we account for the bioplastic as an externally purchased feedstock, rather than included plastic production in the model. Since the final composite contains 70 wt% of this plastic, its price will be strongly tied to the assumed purchase price of the plastic. To identify the other main cost drivers associated with processing the CBP residuals, we first analyzed the minimum selling price (MSP) of the residual fraction contained in the composite. In the model, this was done by setting the cost of the polymer to zero. Analyzing the results in this way allows the results to be agnostic to the choice of bioplastic to be blended, and therefore its cost. The MSP of the blended residual was $1.92 per kg, driven mostly by capital expenses and electricity usage (Fig. 11a). Total capital investment (TCI) was $123 MM; the largest line items were the spray driers (17 required; max throughput was 1360 kg h^{-1}) and homogenizers (26 required; max throughput was 17 gallons per minute). Multiple pieces of equipment were required given the large flowrate through the system, which in turn is determined by the low solids content in the process stream. The large capital requirement is caused by the low solids content, leading to high liquid flow rates through the process (100 m^3 h^{-1}).

The price of the composite depends on the bioplastic purchase price. Blending the processed residuals with the plastic produces a product with a lower selling price so long as the purchase price of the plastic is above the MSP of the blended

 This journal is © The Royal Society of Chemistry 2026

Open Access Article. Published on 21 May 2026. Downloaded on 6/11/2026 11:23:03 PM.
This article is licensed under a Creative Commons Attribution 3.0 Unported Licence.

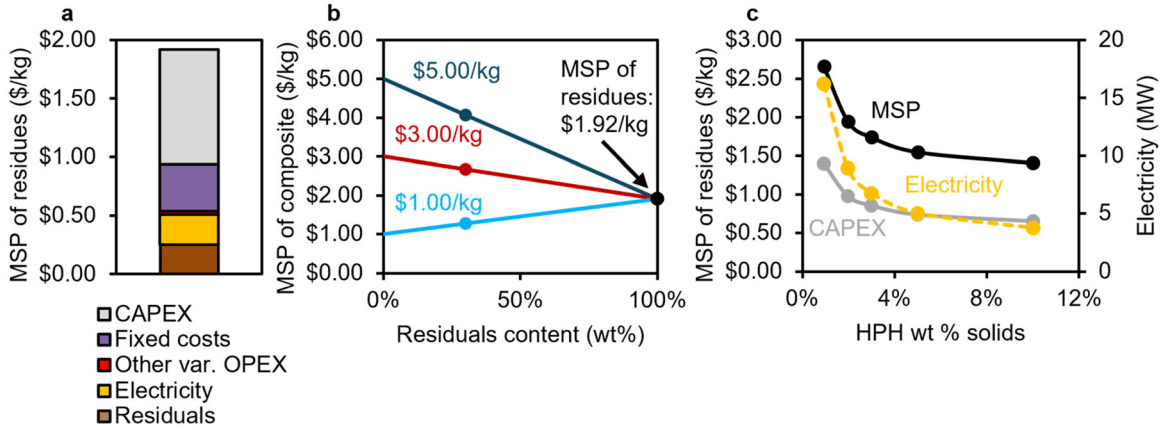

Fig. 11 Economic results for biocomposite production. (a) Breakdown of the MSP of residues. This represents the costs to purchase and process the residual into a blended composite, but does not include the cost of the bioplastic in order to highlight the costs associated with processing. (b) MSP of the final composite, including the bioplastic costs. (c) Impact of the solids loading through high pressure homogenization. CAPEX represents the contribution of CAPEX to the MSP of CBP residues. A solids content of 2% was used in lab studies.

residual ($1.92 per kg). Common plastics such as polypropylene or polyethylene are commonly in the $1–2 per kg range depending on the properties, however specialty/lower volume plastics such as PBS can be closer to $5.00 per kg. At a bioplastic purchase price of $5.00 per kg and a residual blend rate of 30 wt%, the MSP of the composite was reduced to $4.07, highlighting the potential for the use of residuals to lower the composite MSP (Fig. 11b).

Sensitivity analysis identified the solids content in the mixture sent to homogenization as a major driver of process costs. Homogenization units were sized based on the total incoming mixture flowrate, and thus additional water dilution flow requires additional units, increasing the capital expenses. Furthermore, each homogenization unit consumes electricity in correspondence with the total flowrate due to additional pumping energy required. After homogenization, the mechanical vapor recompression evaporator (spray dryer) also requires electricity for operation, and therefore increasing the solids content decreases the energy requirement. Increasing the solids content from 2 wt% to 10 wt% decreases the MSP of the residual contained in the composite from $1.94 per kg to $1.55 per kg and electricity use from 8.9 MW to 3.7 MW (Fig. 11c). Further cost reductions should therefore center on increasing the wt% of solids that can be processed and/or the wt% of the residuals that can be contained in the composite without requiring additional material for the application.

Additionally, we acknowledge that while spray drying was utilized at the laboratory scale to ensure the production of fine, uniform powders for consistent compounding, it represents a significant energy demand. For industrial-scale deployment, spray drying operations could be replaced with high-pressure filtration techniques, which would allow for the rapid mechanical recovery and recycling of process water directly back into the HSH loop, thus significantly reducing thermal loads. The resulting concentrated, homogenized biomass cake can then be dried using low-energy methods, such as stirred air-drying or through the use of waste-heat.

3.9. Life cycle assessment (LCA)

Cradle-to-gate global warming potential (GWP) was calculated for the entire CBP biorefinery and disaggregated by biorefinery input as shown in Fig. 12. The percentage of lignin residuals diverted to bioplastics has little to no effect on biorefinery-level GWP, except when 100% of residuals are diverted. In this scenario, additional natural gas must be purchased for the biorefinery to use in generating process heat and steam, and this input increases the biorefinery-level GWP by roughly 20% compared to the 70% residual diversion scenario.

The biorefinery-level GWP results are allocated between the three biorefinery coproducts (ethanol, electricity, and lignin residuals) using economic allocation to produce the product-level GWP results (Fig. 13a). Economic allocation is applied to divide the gross GWP between the three co-products using the coproduct prices calculated as part of the TEA and given in Table 3.

Fig. 10a shows that ethanol GWP is relatively more sensitive to residual diversion compared to biorefinery-level GWP, but lignin residual and electricity GWP remains fairly insensitive to residual diversion. Both ethanol and lignin residual GWP increases under the 100% residual diversion scenario primarily due to the use of natural gas, a trend analogous to that seen in Fig. 12.

Lignin residual GWP from the 9.4% residual diversion scenario, marked with an asterisk in Fig. 13a, is then used in the composite GWP (Fig. 13b). The results represent a composite consisting of 70 wt% polymer matrix and 30 wt% bone-dry lignin residuals. Also shown is the relatively small contribution to composite GWP of all inputs other than polymer matrix and lignin residuals to the composite manufacturing process (Fig. 13b, green bars). The error bars indicate the variability of

Open Access Article. Published on 21 May 2026. Downloaded on 6/11/2026 11:23:03 PM.
This article is licensed under a Creative Commons Attribution 3.0 Unported Licence.

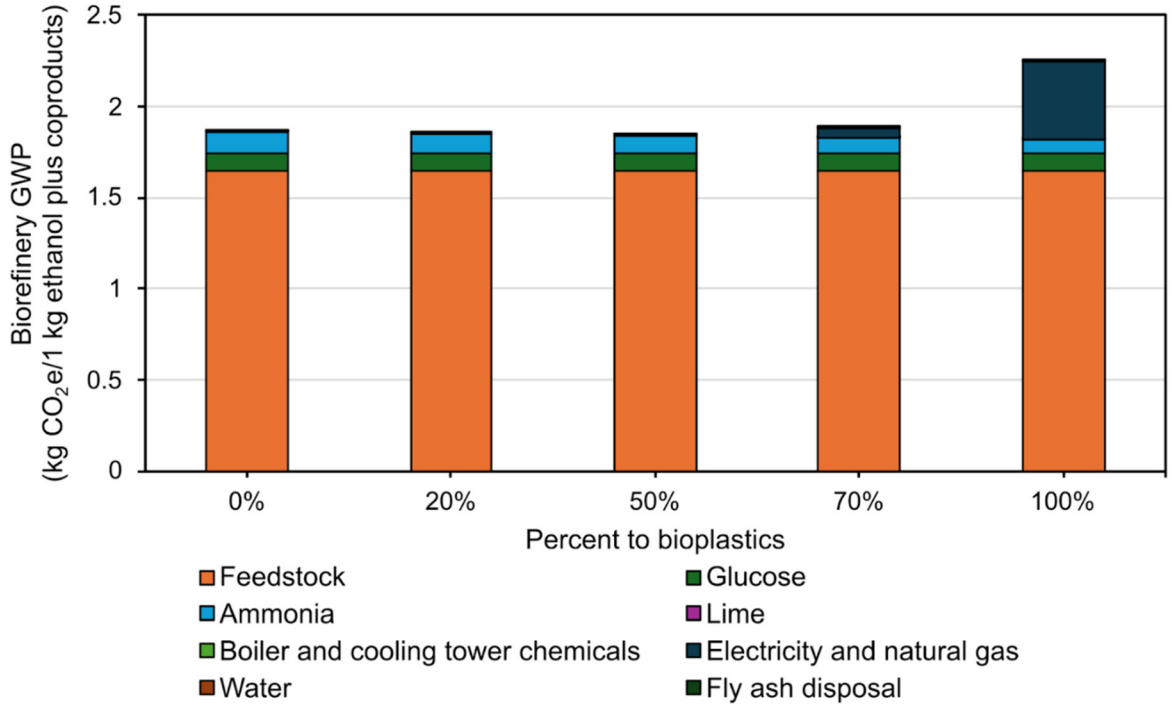

Fig. 12 GWP results for CBP biorefinery operations. Biorefinery-level GWP represents total life cycle emissions associated with the production of 1 kg ethanol plus lignin residual and electricity co-product (if produced), disaggregated by material and energy input to the CBP process. In all residual diversion scenarios, the poplar feedstock (orange) contributes the majority of biorefinery-level GWP. This is due both to the high amount of poplar feedstock required, relative to other biorefinery input amounts, and to the exclusion from the LCA scope of biogenic carbon uptake by growing poplar and agricultural soil. Including carbon uptake would substantially reduce the GWP associated with the poplar feedstock, but as this value is inherently uncertain and difficult to measure, it is not quantified in this study.

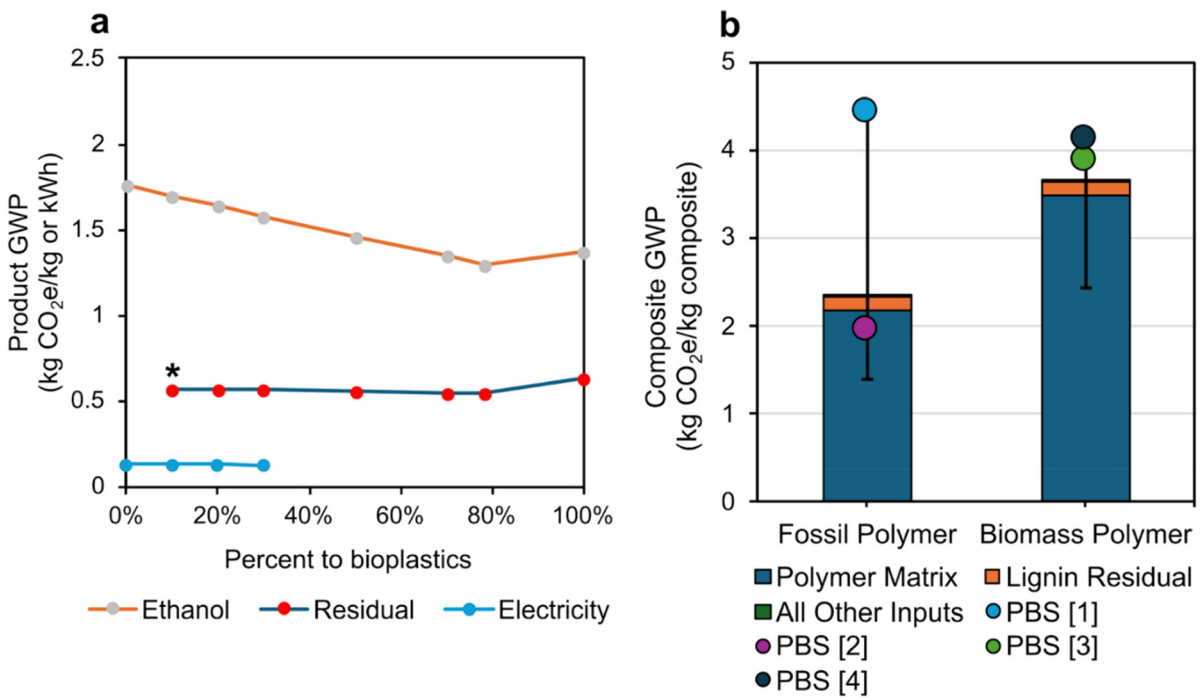

Fig. 13 Product level GWP results. (a) Ethanol, lignin residual, and electricity GWP over a range of lignin residual diversion, calculated from economic allocation. (b) Lignin residual composite GWP and the variability due to choice of polymer matrix (blue columns and colored circles). PBS values [1] and [3] are taken from Tecchio *et al.* (2016),[62] with value [3] representing an average GWP across a variety of biomass feedstocks. PBS value [2] is taken from Ioannidou (2022),[63] and value [4] from Rajendran and Han (2023).[64]

This journal is © The Royal Society of Chemistry 2026

Open Access Article. Published on 21 May 2026. Downloaded on 6/11/2026 11:23:03 PM. This article is licensed under a Creative Commons Attribution 3.0 Unported Licence.

Table 3 Co-product prices used in calculating economic allocation factors

Percent to bioplastics	0%	10%	20%	30%	50%	70%	100%
Ethanol price ($ per kg)	0.77	0.75	0.72	0.70	0.66	0.62	0.54
Residuals price ($ per bone-dry kg)	0.25						
Electricity price ($ per kWh)	0.06						

the polymer matrix GWP due to the choice of polymer matrix (Table 2). GWP values for composites using a polybutylene succinate (PBS) polymer matrix are indicated with circles; each of these circles indicate a PBS GWP from a different recent literature source, and vary due to choice of feedstock, processing technology, and background LCI dataset used. The large variability due to choice of polymer matrix, and the small contribution to composite GWP made by lignin residuals, indicates that further improvements in the CBP biorefinery and supply chain will likely have minimal impact on composite GWP.

4. Conclusions

This study demonstrates a sustainable and scalable pathway for the valorization of consolidated bioprocessing residues from switchgrass and poplar into high-performance, biodegradable biocomposites. Unlike chemical functionalization, which requires precise stoichiometric ratios of lignin and carbohydrate hydroxyl groups to covalently bridge the filler and matrix, HSH facilitates a primarily physical transformation. By mechanically deconstructing recalcitrant cell wall structures into high-aspect-ratio microfibers, HSH creates a high-surface-area interface that promotes mechanical interlocking and ensures exceptional interfacial compatibility with the PBS matrix. Further, we demonstrated that despite the inherent architectural differences between switchgrass and poplar biomass, the resulting biocomposites exhibit comparable reinforcing efficiency. This suggests that HSH effectively homogenizes diverse feedstocks into a uniform reinforcing phase, regardless of their initial structure.

The integration of 30 wt% homogenized CBP residues resulted in a dramatic enhancement of the material's thermomechanical properties. While the exact lignin-to-carbohydrate ratio varies with CBP processes, the natural composite structure of the residue remains resilient. We hypothesize that the slightly higher lignin content of CBP residuals improves interfacial wetting *via* increased hydrophobicity. DMA revealed a 152% increase in storage modulus E' in the rubbery region for PBS/H-CBP-R-SG compared to neat PBS, alongside a significant suppression of the tan δ peak. This restricted segmental mobility proved to be the decisive factor in enabling the transition from injection molding to advanced additive manufacturing. While neat PBS exhibited catastrophic warping and delamination during 3D printing due to high volumetric shrinkage, the biocomposite filaments demonstrated excellent dimensional stability and interlayer adhesion, allowing for the use of standard PLA printing profiles. Furthermore, the refined HSH microfibers served as a dual-purpose agent, providing a structural scaffold for mechanical performance during the intended regular use cases, and acting as a hydrophilic network for moisture and microbial ingress during the end-of-life phase.

TEA further supports the commercial viability of this approach, identifying solids content and pumping energy during homogenization as key drivers for cost optimization. Overall, this work provides a robust framework for converting agricultural and industrial waste into circular bioplastics that meet the rigorous demands of modern 3D printing while ensuring rapid environmental return, effectively bridging the gap between high-tech manufacturing and sustainable waste management.

Abbreviations

ASTM	American Society for Testing and Materials
BESC	BioEnergy Science Center
CBI	Center for Bioenergy Innovation
CBP	Consolidated bioprocessing
CBP-R	Consolidated bioprocessing residuals
CBP-R-P	Poplar consolidated bioprocessing residues
CBP-R-SG	Switchgrass consolidated bioprocessing residues
CM	Cyclone mill
CM-CBP-R	Cyclone milled consolidated bioprocessing residues
CM-CBP-R-P	Cyclone milled poplar consolidated bioprocessing residues
CM-CBP-R-SG	Cyclone milled switchgrass consolidated bioprocessing residues
DSC	Differential scanning calorimetry
DTG	Derivative thermogravimetric
FDM	Fused Deposition Modeling
GGE	Gallons of gasoline equivalent
GWP	Global warming potential
H-CBP-R	Homogenized consolidated bioprocessing residues
H-CBP-R-P	Homogenized poplar consolidated bioprocessing residues
H-CBP-R-SG	Homogenized switchgrass consolidated bioprocessing residues
HPH	High pressure homogenizer
HSH	High shear homogenizer
LC	Lignocellulosic biomass
LCA	Life cycle assessment
LCI	Life cycle inventory
MESP	Minimum ethanol selling price
MFI/MFR	Melt flow index (OR) melt flow rate
MSP	Minimum selling price
MTC	Thermophilic Clostridia
NLR	National Laboratory of the Rockies
PB	Poplar biomass

PBAT	Poly (butylene adipate terephthalate)
PBS	Poly (butylene succinate)
PLA	Poly (lactic acid)
SEM	Scanning electron microscopy
SGB	Switchgrass biomass
TCI	Total capital investment
TEA	Techno-economic analysis
TGA	Thermogravimetric analysis

Open Access Article. Published on 21 May 2026. Downloaded on 6/11/2026 11:23:03 PM.
This article is licensed under a Creative Commons Attribution 3.0 Unported Licence.

Author contributions

NSY conceived the study, designed the overall research concept, performed experiments, and contributed to drafting the manuscript. MA conducted experiments and contributed to manuscript drafting. NNH prepared the consolidated bioprocessing (CBP) residuals and contributed to drafting the manuscript. DCJ supported the execution of the 3D printing experiments. JD, JKK, and RJH carried out process simulation, TEA, and LCA, and contributed to drafting the manuscript. BCK supervised the process simulation, TEA, and LCA work, and contributed to manuscript drafting. YJB supervised the consolidated bioprocessing work and CBP residual preparation. KGP supported composite material preparation and contributed to drafting the manuscript. JJL provided access to the New Materials Institute facilities for materials analysis and composite fabrication. SM provided scientific discussions and contributed to drafting the manuscript. BRU oversaw the overall project, secured funding, and contributed to drafting the manuscript.

Conflicts of interest

There are no conflicts to declare.

Data availability

The supporting data has been provided as part of the supplementary information (SI). Table S1: LCI dataset for the CBP biorefinery. Table S2: LCI dataset for composite production. Table S3: Tensile and impact strength test analysis of PBS and composites. Table S4: Benchmarking mechanical properties against common thermolastics. Fig. S1: Composting setup and sample placement for biodegradability assessment of PBS and PBS/H-CBP-R-SG biocomposites. Fig. S2: SEM of HSH treated CBP-R-P sample. See DOI: https://doi.org/10.1039/d6gc00489j.

Acknowledgements

This work was authored in part by the National Laboratory of the Rockies for the U.S. Department of Energy (DOE), operated under Contract No. DE-AC36-08GO28308. Funding was provided by the Center for Bioenergy Innovation supported by the U.S. Department of Energy, Office of Science, Biological and Environmental Research under Contract Number ERKP886. Oak Ridge National Laboratory is managed by UT-Battelle, LLC for the U.S. Department of Energy under contract no. DE-AC05-00OR22725. S.M. acknowledges the NSF award CMMI-EPSRC 2401713. B.R.U and M.A. would also like to acknowledge the BioPoplar initiative supported by U.S. Department of Energy, Office of Science, Office of Biological and Environmental Research program under Award Number DE-SC0023338. The views expressed in the article do not necessarily represent the views of the DOE or the U.S. Government. The U.S. Government retains and the publisher, by accepting the article for publication, acknowledges that the U.S. Government retains a nonexclusive, paid-up, irrevocable, worldwide license to publish or reproduce the published form of this work, or allow others to do so, for U.S. Government purposes.

References

1 U. Kong, N. F. M. Rawi and G. S. Tay, *Polymers*, 2023, **15**, 2399.
2 B. Mylsamy, S. K. M. Shanmugam, K. Aruchamy, S. Palanisamy, R. Nagarajan and N. Ayrilmis, *Polym. Eng. Sci.*, 2024, **64**, 2345–2373.
3 I. McKay, J. Vargas, L. Yang and R. M. Felfel, *Materials*, 2024, **17**, 4878.
4 M. Jawaid, M. T. Paridah and N. Saba, in *Lignocellulosic Fibre and Biomass-Based Composite Materials*, ed. M. Jawaid, P. Md Tahir and N. Saba, Woodhead Publishing, 2017, pp. 1–11.
5 K. O. Iwuozor, V. E. Ojukwu, S. O. Eshiemogie, E. C. Emenike, A. O. Bajeh, J. O. Ighalo and A. G. Adeniyi, in *Plant Biomass Applications*, ed. M. Jawaid, A. Khan and A. M. Ahmed Asiri, Academic Press, 2024, pp. 385–405.
6 U. Qasim, M. Ali, T. Ali, R. Iqbal and F. Jamil, *ChemBioEng Rev.*, 2020, **7**, 193–215.
7 A. A. Adeleke, P. P. Ikubanni, T. A. Orhadahwe, C. T. Christopher, J. M. Akano, O. O. Agboola, S. O. Adegoke, A. O. Balogun and R. A. Ibikunle, *Heliyon*, 2021, **7**, e08025.
8 D. C. Josey, N. S. Yadavalli, J. C. Moore, M. J. Peña, S. Minko and B. R. Urbanowicz, *Biotechnol. Sustainable Mater.*, 2024, **1**, 9.
9 H. S. Kim, E. M. White, G. Crane, K. Patel, M. H. Noh, M. A. Rahman, A. M. Feist, J. J. Locklin and J. K. Pokorski, *Chem. Eng. J.*, 2025, **505**, 159863.
10 M. J. Mochane, S. I. Magagula, J. S. Sefadi and T. C. Mokhena, *Polymers*, 2021, **13**, 1200.
11 J. Li, D. J. W. Lawton, G. G. Sacripante, M. R. Thompson and H. S. Marway, *Ind. Eng. Chem. Res.*, 2021, **60**, 13886–13894.
12 K. Müller, C. Zollfrank and M. Schmid, *Macromol. Mater. Eng.*, 2019, **304**, 1800760.

 This journal is © The Royal Society of Chemistry 2026

Open Access Article. Published on 21 May 2026. Downloaded on 6/11/2026 11:23:03 PM. This article is licensed under a Creative Commons Attribution 3.0 Unported Licence.

13 O. Platnieks, S. Gaidukovs, A. Barkane, G. Gaidukova, L. Grase, V. K. Thakur, I. Filipova, V. Fridrihsone, M. Skute and M. Laka, *Molecules*, 2020, **25**, 121.
14 F. Berzin, C. David and B. Vergnes, *Front. Mater.*, 2020, **7**, 218.
15 R. M. Rowell, *J. Polym. Environ.*, 2007, **15**, 229–235.
16 F. H. Isikgor and C. R. Becer, *Polym. Chem.*, 2015, **6**, 4497–4559.
17 E. D. Flores, M. Funabashi and M. Kunioka, *J. Appl. Polym. Sci.*, 2009, **112**, 3410–3417.
18 A. Ayoub, T. Treasure, L. Hansen, T. Nypelö, H. Jameel, S. Khan, H. Chang, M. A. Hubbe and R. A. Venditti, *Cellulose*, 2021, **28**, 1039–1053.
19 Y. Zhang, S. Zhou, X. Fang, X. Zhou, J. Wang, F. Bai and S. Peng, *Eur. Polym. J.*, 2019, **116**, 265–274.
20 L. N. Horiuchi, F. D. P. M. Torres, R. Barbosa, J. B. Azevedo, F. Garcia-Villen, C. Viseras, R. De Melo Barbosa and R. Fialho, *J. Appl. Polym. Sci.*, 2025, **142**, e57543.
21 M. Zhou, J. Yan, Y. Li, C. Geng, C. He, K. Wang and Q. Fu, *RSC Adv.*, 2013, **3**, 26418–26426.
22 T. H. Nam, S. Ogihara, S. Kobayashi and K. Goto, *Adv. Compos. Mater.*, 2015, **24**, 161–178.
23 H. Wu, F. Sun, R. Liu and C. Li, *J. Thermoplast. Compos. Mater.*, 2024, **37**, 3616–3629.
24 A. Scoma, L. Bertin, M. A. M. Reis, M. Kornaros and M. Coma, *BioMed Res. Int.*, 2016, **2016**, 4327575.
25 J. A. Poveda-Giraldo, S. Piedrahita-Rodríguez and C. A. Cardona Alzate, *Chem. Eng. Trans.*, 2021, **83**, 397–402.
26 M. H. Langholtz, C. Brandt, R. Clark, H. Cook, S. Curran, M. Davis, D. De La Torre Ugarte, R. Efroymson, J. Field, C. Hellwinckel, R. Jacobson, K. L. Kline, O. Oyedeji, E. Parish, E. Schmidt, T. Theiss, A. Badgett, B. Klein, A. Milbrandt, M. R. Wiatrowski, T. Hawkins, L. Ou, U. Singh, J. Zhang, A. Coleman, S. Gao, L. Miller, T. Saltiel, L. Snowden-Swan, P. Valdez, Y. Xu, Y. Zhu, B. English, L. Lambert, K. Davis, J. De angelo, R. Abt, D. Rossi, K. Abt, C. Brandeis, J. Fried, P. Nepal, J. Prestemon, K. Champion, A. Otwell, B. Saenz, E. Harrison, C. O'dea, G. Cooney, J. Hoffmann, M. Shell, R. Davis and L. Walker, 2023 Billion-Ton Report: An Assessment of U.S. Renewable Carbon Resources, 2024, United States. DOI: 10.2172/2441098.
27 I. U. Zambello, E. K. Holwerda and L. R. Lynd, *Bioresour. Technol.*, 2024, **406**, 130973.
28 M. R. Kubis, E. K. Holwerda and L. R. Lynd, *Biotechnol. Biofuels Bioprod.*, 2022, **15**, 12.
29 S. Ghosh, E. K. Holwerda, R. S. Worthen, L. R. Lynd and B. P. Epps, *Biotechnol. Biofuels*, 2018, **11**, 246.
30 A. Anstey, S. Muniyasamy, M. M. Reddy, M. Misra and A. Mohanty, *J. Polym. Environ.*, 2014, **22**, 209–218.
31 L. Aliotta, M. Seggiani, A. Lazzeri, V. Gigante and P. Cinelli, *Polymers*, 2022, **14**, 844.
32 Y. Tachibana, T. Masuda, M. Funabashi and M. Kunioka, *Biomacromolecules*, 2010, **11**, 2760–2765.
33 P. R. Makgwane, S. Muniyasamy, L. Hlekelele, A. Swanepoel, V. S. Sypu, L. Mdlalose, S. Naidoo, Z. Cele, A. Maity, M. Balogun and O. J. Botlhoko, *J. Renewable Mater.*, 2025, **13**, 449–495.
34 V. Rajgond, A. Mohite, N. More and A. More, *Polym. Bull.*, 2024, **81**, 5703–5752.
35 S. A. Rafiqah, A. Khalina, A. S. Harmaen, I. A. Tawakkal, K. Zaman, M. Asim, M. N. Nurrazi and C. H. Lee, *Polymers*, 2021, **13**, 1436.
36 S. Sahoo, M. Misra and A. K. Mohanty, *Macromol. Mater. Eng.*, 2014, **299**, 178–189.
37 M. I. Peñas, R. A. Pérez-Camargo, R. Hernández and A. J. Müller, *Polymers*, 2022, **14**, 1025.
38 Z. Liang, P. Pan, B. Zhu, T. Dong and Y. Inoue, *J. Appl. Polym. Sci.*, 2010, **115**, 3559–3567.
39 P. Pei, Y. Sun, R. Zou, X. Wang, J. Liu, L. Liu, X. Deng, X. Li, M. Yu and S. Li, *BioResources*, 2023, **18**, 7154–7171.
40 P. Liminana, D. Garcia-Sanoguera, L. Quiles-Carrillo, R. Balart and N. Montanes, *Composites, Part B*, 2018, **144**, 153–162.
41 T. H. Nam, S. Ogihara, N. H. Tung and S. Kobayashi, *J. Solid Mech. Mater. Eng.*, 2011, **5**, 251–262.
42 T. H. Nam, S. Ogihara, H. Nakatani, S. Kobayashi and J. I. Song, *Adv. Compos. Mater.*, 2012, **21**, 241–258.
43 M. Shibata, R. Makino, R. Yosomiya and H. Takeishi, *Polym. Polym. Compos.*, 2001, **9**, 333–338.
44 K. Papadopoulou, P. A. Klonos, A. Kyritsis, O. Mašek, C. Wurzer, K. Tsachouridis, A. D. Anastasiou and D. N. Bikiaris, *Polymers*, 2023, **15**, 1049.
45 F. Olivieri, R. Capuano, A. Pirozzi, R. Castaldo, R. Avolio, M. E. Errico, C. Licini, S. Garzoli, G. Spigno, F. Donsì and G. Gentile, *ACS Sustainable Chem. Eng.*, 2025, **13**, 5121–5130.
46 K. P. Root, A. K. Pal, E. Pesaranhajiabbas, A. K. Mohanty and M. Misra, *Composites, Part C*, 2023, **11**, 100358.
47 R. P. Araújo, C. A. G. Beatrice, E. H. Backes and L. C. Costa, *Polym. Compos.*, 2024, **45**, 13650–13662.
48 A. Soni, S. K. Gupta, D. Veeman and J. K. Katiyar, *Environ. Sci. Pollut. Res.*, 2025, **32**, 28559–28605.
49 R. P. Araújo, C. A. G. Beatrice, E. H. Backes and L. C. Costa, *Polym. Compos.*, 2024, **45**, 13650–13662.
50 B. Niang, N. Schiavone, H. Askanian, V. Verney, D. Ndiaye and A. B. Diop, *Materials*, 2022, **15**, 7570.
51 S. Zhou and A. N. Hrymak, *Polymers*, 2024, **16**, 1796.
52 P. T. Anastas and J. C. Warner, *Green Chemistry: Theory and Practice*, Oxford University Press, Oxford, New York, 2000.
53 Z. R. King, A. L. Bray, P. R. LaFayette and W. A. Parrott, *Plant Cell Rep.*, 2014, **33**, 313–322.
54 H. Akinosho, K. Yee, M. Rodriguez, W. Muchero, C. G. Yoo, M. Li, O. Thompson, Y. Pu, S. Brown, J. Mielenz and A. J. Ragauskas, *ChemistrySelect*, 2017, **2**, 10642–10647.
55 E. K. Holwerda, K. D. Hirst and L. R. Lynd, *J. Ind. Microbiol. Biotechnol.*, 2012, **39**, 943–947.
56 E. K. Holwerda, K. D. Hirst and L. R. Lynd, *J. Ind. Microbiol. Biotechnol.*, 2012, **39**, 943–947.

Open Access Article. Published on 21 May 2026. Downloaded on 6/11/2026 11:23:03 PM. This article is licensed under a Creative Commons Attribution 3.0 Unported Licence.

57 J. Sluiter and A. Sluiter, *NREL, NREL/TP-510-48087*, 2010, pp. 1–10.
58 D. Humbird, R. Davis, L. Tao, C. Kinchin, D. Hsu, A. Aden, P. Schoen, J. Lukas, B. Olthof, M. Worley, D. Sexton and D. Dudgeon, *Process Design and Economics for Biochemical Conversion of Lignocellulosic Biomass to Ethanol: Dilute-Acid Pretreatment and Enzymatic Hydrolysis of Corn Stover*, 2011.
59 L. R. Lynd, X. Liang, M. J. Biddy, A. Allee, H. Cai, T. Foust, M. E. Himmel, M. S. Laser, M. Wang and C. E. Wyman, *Curr. Opin. Biotechnol.*, 2017, **45**, 202–211.
60 Intergovernmental Panel on Climate Change (IPCC), *Climate Change 2021 – The Physical Science Basis: Working Group I Contribution to the Sixth Assessment Report of the Intergovernmental Panel on Climate Change*, Cambridge University Press, Cambridge, 2023.
61 DATASMART Life Cycle Inventory – Long Trail Sustainability, https://longtrailsustainability.com/software/datasmart-life-cycle-inventory/, (accessed November 3, 2025).
62 P. Tecchio, P. Freni, B. De Benedetti and F. Fenouillot, *J. Cleaner Prod.*, 2016, **112**, 316–325.
63 S. M. Ioannidou, D. Ladakis, E. Moutousidi, E. Dheskali, I. K. Kookos, I. Câmara-Salim, M. T. Moreira and A. Koutinas, *Sci. Total Environ.*, 2022, **806**, 150594.
64 N. Rajendran and J. Han, *Waste Manage.*, 2023, **156**, 168–176.
65 R. J. Hanes, R. J. Clark, B. C. Klein, J. L. Field, E. G. Webb and B. H. Davison, *Biofuels, Bioprod. Biorefin.*, 2026, **20**, 20–26.
66 M. Akter, Md. H. Uddin and H. R. Anik, *Polym. Bull.*, 2024, **81**, 1–85.
67 A. Gaikwad and A. Meshram, *Chem. Eng. Commun.*, 2020, **207**, 1696–1706.
68 J. Joy, C. Jose, S. B. Varanasi, L. P. Mathew and S. Pilla, *J. Renewable Mater.*, 2016, **4**, 351–364.
69 H. Taheri and P. Samyn, *Cellulose*, 2016, **23**, 1221–1238.
70 W. Xia, L. Shao, C. Wang, Y. Liu, X. Zeng and F. Xu, *Green Chem.*, 2025, **27**, 2056–2064.
71 Y. Kim, N. S. Mosier and M. R. Ladisch, *Biotechnol. Prog.*, 2009, **25**, 340–348.
72 R. A. Smith and J. Ralph, *Nat. Plants*, 2024, **10**, 1284–1286.
73 S. Pivsa-Art and W. Pivsa-Art, *Polym. Compos.*, 2021, **42**, 1752–1759.
74 S. Torres, R. Navia, R. C. Murdy, P. Cooke, M. Misra and A. K. Mohanty, *ACS Sustainable Chem. Eng.*, 2015, **3**, 614–624.
75 *Vibration and Damping Behavior of Biocomposites*, ed. S. M. K. Thiagamani, M. E. Hoque, S. Krishnasamy, C. Muthukumar and S. Siengchin, CRC Press, Boca Raton, 2022.
76 S. Chauhan, A. Karmarkar and P. Aggarwal, *J. Appl. Polym. Sci.*, 2009, **114**, 2421–2426.
77 T. Venkategowda, L. H. Manjunatha and P. R. Anilkumar, *Mater. Today. Proc.*, 2022, **54**, 395–401.
78 C. M. Chan, L.-J. Vandi, S. Pratt, P. Halley, D. Richardson, A. Werker and B. Laycock, *Polym. Rev.*, 2018, **58**, 444–494.
79 D. M. de Carvalho, J. Berglund, C. Marchand, M. E. Lindström, F. Vilaplana and O. Sevastyanova, *Carbohydr. Polym.*, 2019, **220**, 132–140.
80 M. V. Ramiah, *Appl. Polym. Sci.*, 1970, **14**, 1323–1337.
81 E. A. Varol and Ü. Mutlu, *Energies*, 2023, **16**, 3674.
82 L. Gašparovič, Z. Koreňová and Ľ. Jelemenský, *Chem. Pap.*, 2010, **64**, 174–181.
83 C. Marcuello, B. Chabbert, F. Berzin, N. B. Bercu, M. Molinari and V. Aguié-Béghin, *Materials*, 2023, **16**, 2440.
84 S. Sahoo, M. Misra and A. K. Mohanty, *J. Appl. Polym. Sci.*, 2013, **127**, 4110–4121.
85 H. A. Saffian, K. Hyun-Joong, P. M. Tahir, N. A. Ibrahim, S. H. Lee and C. H. Lee, *Materials*, 2019, **12**, 4043.
86 M. Tajvidi and A. Takemura, *Polym. Compos.*, 2009, **30**, 1226–1233.
87 S. A. Rafiqah, A. Khalina, A. S. Harmaen, I. A. Tawakkal, K. Zaman, M. Asim, M. N. Nurrazi and C. H. Lee, *Polymers*, 2021, **13**, 1436.
88 W. Hu, M. Zou, S. Zhang, B. Yang and Y. Cang, *J. Phys. D: Appl. Phys.*, 2025, **58**, 183001.
89 J. Y. Boey, C. K. Lee and G. S. Tay, *Polymers*, 2022, **14**, 3737.
90 T. Vu-Khanh, *Polymer*, 1988, **29**, 1979–1984.
91 K. Ishii, M. Fukui and S. Takii, *J. Appl. Microbiol.*, 2000, **89**, 768–777.
92 M. K. Iqbal, T. Shafiq and K. Ahmed, *Environ. Technol.*, 2010, **31**, 205–214.
93 T. Zhiltsova, J. Campos, A. Costa and M. S. A. Oliveira, *Materials*, 2024, **17**, 696.
94 M. N. A. M. Taib and N. M. Julkapli, in *Mechanical and Physical Testing of Biocomposites, Fibre-Reinforced Composites and Hybrid Composites*, ed. M. Jawaid, M. Thariq and N. Saba, Woodhead Publishing, 2019, pp. 61–79.
95 W. S. DePolo, *Dimensional Stability and Properties of Thermoplastics Reinforced with Particulate and Fiber Fillers*, Virginia Tech, 2005.
96 M. R. Kubis and L. R. Lynd, *Sustainable Energy Fuels*, 2023, **7**, 3842–3852.
97 R. Davis, L. Tao, E. Tan, G. Beckham, D. Humbird, D. Thompson, M. Roni, N. Grundl and M. Biddy, Process Design and Economics for the Conversion of Lignocellulosic Biomass to Hydrocarbon Fuels and Coproducts: 2018 Biochemical Design Case Update; Biochemical Deconstruction and Conversion of Biomass to Fuels and Products *via* Integrated Biorefinery Pathways, 2018, DOI: 10.2172/1483234.
98 A. H. Tullo, *The biodegradable polymer PBAT is hitting the big time*, 2021, **99**, 34, https://cen.acs.org/business/bio-based-chemicals/biodegradable-polymer-PBAT-hitting-big/99/i34.
99 S.-M. Ioannidou, D. Ladakis, R. Rebolledo-Leiva, S. G. García, M. T. Moreira, I. K. Kookos and A. Koutinas, in *Computer Aided Chemical Engineering*, ed. A. C. Kokossis, M. C. Georgiadis and E. Pistikopoulos, Elsevier, 2023, vol. 52, pp. 2515–2520.
100 Univation Technologies Announces World-Scale 800 000 Tonnes/Year Design Capacity for UNIPOLTM PE Process

This journal is © The Royal Society of Chemistry 2026

Technology, https://www.univation.com/en-us/news-and-events/univation-technologies-announce-world-scale-toones-year-design.html, (accessed October 21, 2025).

101 R. Davis, T. Hawkins, A. Coleman, S. Gao, B. Klein, M. Wiatrowski, Y. Zhu, Y. Xu, L. Snowden-Swan, P. Valdez, J. Zhang, U. Singh and L. Ou, *Economic, Greenhouse Gas, and Resource Assessment for Fuel and Protein Production from Microalgae: 2022 Algae Harmonization Update*, 2024.

102 R. Davis, L. Tao, E. C. D. Tan, M. J. Biddy, G. T. Beckham, C. Scarlata, J. Jacobson, K. Cafferty, J. Ross, J. Lukas, D. Knorr and P. Schoen, *Process Design and Economics for the Conversion of Lignocellulosic Biomass to Hydrocarbons: Dilute-Acid and Enzymatic Deconstruction of Biomass to Sugars and Biological Conversion of Sugars to Hydrocarbons*, National Renewable Energy Laboratory (NREL), Golden, CO, United States, 2013.

Open Access Article. Published on 21 May 2026. Downloaded on 6/11/2026 11:23:03 PM.
This article is licensed under a Creative Commons Attribution 3.0 Unported Licence.